Damp heat-stable perovskite solar cells with tailored-dimensionality 2D/3D heterojunctions.

Item Type	Article
Authors	Azmi, Randi; Ugur, Esma; Seitkhan, Akmaral; Aljamaan, Faisal; Subbiah, Anand Selvin; Liu, Jiang; Harrison, George T; Nugraha, Mohamad Insan; Eswaran, Mathan Kumar; Babics, Maxime; Chen, Yuan; Xu, Fuzong; Allen, Thomas; Rehman, Atteq Ur; Wang, Chien-Lung; Anthopoulos, Thomas D.; Schwingenschlögl, Udo; de Bastiani, Michele; Aydin, Erkan; De Wolf, Stefaan
Citation	Azmi, R., Ugur, E., Seitkhan, A., Aljamaan, F., Subbiah, A. S., Liu, J., Harrison, G. T., Nugraha, M. I., Eswaran, M. K., Babics, M., Chen, Y., Xu, F., Allen, T. G., Rehman, A. ur, Wang, C.-L., Anthopoulos, T. D., Schwingenschlögl, U., De Bastiani, M., Aydin, E., & De Wolf, S. (2022). Damp heat–stable perovskite solar cells with tailored-dimensionality 2D/3D heterojunctions. Science, 376(6588), 73–77. https://doi.org/10.1126/science.abm5784
Eprint version	Post-print
DOI	10.1126/science.abm5784
Publisher	American Association for the Advancement of Science (AAAS)
Journal	Science (New York, N.Y.)
Rights	This is an accepted manuscript of an article published in final form in Science. The final, published version can be accessed at https://www.science.org/doi/10.1126/science.abm5784
Download date	01/10/2023 15:35:44

| Link to Item | http://hdl.handle.net/10754/676541 |

Damp-heat stable perovskite solar cells with tailored dimensionality 2D/3D heterojunctions

Randi Azmi[1], Esma Ugur[1], Akmaral Seitkhan[1], Faisal Aljamaan[1], Anand S. Subbiah[1], Jiang Liu[1], George T. Harisson[1], Mohamad I. Nugraha[1], Mathan K. Eswaran[1], Maxime Babics[1], Yuan Chen[2], Fuzong Xu[1], Thomas G. Allen[1], Atteq ur Rehman[1], Chien-Lung Wang[2], Thomas D. Anthopoulos[1], Udo Schwingenschlögl[1], Michele De Bastiani[1], Erkan Aydin[1], Stefaan De Wolf[1]*

[1]King Abdullah University of Science and Technology (KAUST), KAUST Solar Center (KSC), Physical Sciences and Engineering Division (PSE); Thuwal 23955-6900, Kingdom of Saudi Arabia
[2]Department of Applied Chemistry, National Yang Ming Chiao Tung University; 1001 Ta Hsueh Road, Hsin-Chu, Taiwan

*Corresponding author. Email: stefaan.dewolf@kaust.edu.sa

Abstract:

In order for perovskite solar cells (PSCs) with high power conversion efficiencies (PCEs) to be commercialized, they must achieve long-term stability, which is usually assessed with accelerated degradation tests. One of the persistent obstacles for PSCs has been successfully passing the damp-heat test (85 Celsius and 85% relative humidity), which is standard to verify the stability of commercial photovoltaic (PV) modules. Here, we fabricate damp-heat stable PSCs by tailoring the dimensional fragments of 2D-perovskite layers, formed at room temperature with oleylammonium-iodide molecules, that passivate the perovskite surface at the electron-selective contact. The resulting inverted PSCs deliver a 24.3% PCE and retain >95% of their initial value after >1000 hours at damp-heat test conditions, thereby meeting one of the critical industrial stability standards for PV modules.

One Sentence Summary: Tailoring the dimensionality of 2D-perovskite passivation layers enables efficient and damp-heat stable inverted perovskite solar cells.

Main Text:

Commercialization of any photovoltaic (PV) technology requires a guarantee of the product's lifetime, which is at least 25 to 30 years for conventional crystalline-silicon (c-Si) modules. Lifetime predictions of PV technologies are usually accomplished through standardized accelerated degradation tests. After the demonstration of excellent power conversion efficiencies (PCEs) of perovskite solar cells (PSCs), the main challenge toward market entry of PSCs is successfully passing standard industrial lifetime-assessment tests of the International Electrotechnical Commission (IEC 61215:2016), in particular, damp-heat testing at 85°C and 85% relative humidity (RH) (*1, 2*). A stabilized PCE performing like a commercial c-Si solar cells (PCE ~20%) would need to pass a damp-heat test for >1000 hours with <5% absolute loss in PCE (*3, 4*).

Degradation of encapsulated PSCs is usually caused by leakage in the packaging (allowing atmospheric agents to interact with the perovskite) and device-related material instabilities. To address this, we developed leakage-free device packaging that seals the perovskite within two glass sheets, using a vacuum-laminated encapsulant and edge-sealing via butyl rubber. Despite this, damp-heat testing of our encapsulated control devices resulted in fast degradation (see below), implying an intrinsic thermal instability of the perovskite absorber layer itself.

The instability of three-dimensional (3D) perovskite films, as used as the photo-active absorber layer in PSCs, is mainly attributed to high defect densities as well as ion migration at grain boundaries and interfaces, exacerbated at higher operational temperatures (*5-9*). Several approaches have been reported to passivate these defects (*7, 10-13*). Specifically, growing two-dimensional (2D) perovskite layers on the top surface of 3D-perovskites creates a 2D/3D perovskite heterojunction that can effectively passivate surface defects and suppress ion migration (*3, 6, 14-18*).

At the device level, integrating such 2D-perovskite passivation layers in PSCs can enhance their PCE and lifetime (*3, 4, 14-17*). So far, this strategy has been most successful for regular structured PSCs in which phase-pure 2D-perovskites ($n =1$, n represents the dimensionality of the 2D-perovskite, by counting the number of its octahedral inorganic sheets) were inserted between the 3D-perovskite surface and the (opaque) hole-selective top-contact stack (*3, 14-17*). For inverted devices, this top-contact passivation approach (now at the electron-selective side) has consistently failed in PCE and lifetime and represents a persistent challenge in the perovskite community (*19, 20*), as inverted PSCs are arguably easier to fabricate and scale-up (*11*).

We found that tailoring the dimensionality (n) of the 2D-perovskite fragments at the electron-selective interface of inverted PSCs is essential to enable efficient top-contact passivation through 2D-perovskite passivation layers. This interface has frequently been ignored because it is assumed that the conventional electron-selective layer, C_{60} (or its derivatives), provides sufficient passivation of 3D perovskites (*21*), and instead attention has predominantly focused on the hole-selective interface of inverted PSCs, situated at the (transparent) bottom contact of the device (*22-25*). However, recent reports have revealed that C_{60} is only weakly bonded to perovskite layers, which induces a high energetic disorder between perovskite and C_{60} layers that limits device performance at elevated operating temperatures (*5, 6, 26*). Moreover, a thin layer of C_{60} is insufficient to effectively protect the 3D-perovskite film underneath from moisture or oxygen ingress. Implementing 2D-perovskite passivation layers is a promising approach to solve all of the issues mentioned above.

We post-treated the surface defects of the 3D-perovskites by applying oleylammonium-iodide (OLAI) molecules to form Ruddlesden-Popper phase 2D-perovskite layers, which resulted in higher PCEs and prolonged stabilities of inverted PSCs. We tailored the dimensionality, n, of the 2D-perovskite fragments (which also dictates their optical and electronic properties) by tuning the annealing conditions from lower to higher temperatures, in that higher-n layers have a lower formation energy (27). Indeed, all 2D-perovskite passivation layers prepared through thermal annealing (2D–TA) showed a dominant emission peak at ~510 nm (as evidenced in figure S1), which belongs to $n = 1$, in accordance with previous studies (4, 6, 19, 28). However, the formation of higher-dimensionality 2D-perovskite layers ($n \geq 2$) became more pronounced when the post-treatment was performed at room temperature (2D–RT) with the OLAI molecule (Fig. 1A).

We investigated the formation of 2D-perovskite passivation films on 3D-perovskites with grazing-incidence wide-angle X-ray scattering (GIWAXS, Fig. 1, B and C). The 2D-perovskite passivation films exhibited diffraction q_z peaks at ~0.2 A^{-1} to ~0.5 A^{-1}, corresponding to the (001) and (002) planes of 2D-perovskite crystals (28). As expected, the 2D–TA films were dominated by $n = 1$ layers (with a prominent peak at q_z ~0.35 A^{-1}). In contrast, 2D-RT films exhibited the diffraction peaks of $n = 1$ and 2 with a more substantial $n = 2$ peak at lower q_z (16). The strong intensity in the z-direction for 2D-perovskite films was indicative of a highly oriented lateral direction of the top 3D-perovskite layers.

Cross-sectional high-resolution scanning transmission electron microscopy (HR-STEM) images also showed $n = 1$ and 2 layers in 2D–RT samples (Fig. 1D and figure S2A) but only $n = 1$ in 2D-TA (figure S2C), which is consistent with the GIWAXS results. To differentiate between $n = 1$ and 2 layers, we performed elemental mapping images and profiling positions of 2D-perovskite layers, and Fig. 1E and figure S2B show two-dimensionalities of 2D-layers in 2D-RT samples as the reduction of the density of C, Pb, and I elements, which correspond to $n = 1$ and 2 layers. In comparison, 2D-TA samples showed only $n = 1$ (figure S2D). Further, profiling position of 2D-perovskites from TEM images confirmed the dimensionality of $n = 2$ and 1 by analyzing average distances between two-closest octahedral inorganic sheets. As a result, higher dimensionality ($n = 2$) had a wider distance (~1.5 nm) compared to $n = 1$ (~1.2 nm) (figure S2, E-H).

Scanning electron microscopy (SEM) top-view images revealed that the surface morphology of the perovskite films after 2D-perovskite passivation did not change substantially (figure S3, A-B). Further, the 2D-perovskite passivation films exhibited stronger photoluminescence (PL) emission with a longer PL decay lifetime than control 3D-perovskite films because of the suppression of nonradiative recombination associated with trap states at the surface (figures S4 and S5). Interestingly, the 2D-perovskite ($n = 2$) capping layer formed uniformly on top of 3D-perovskite surfaces for 2D–RT, as shown in the PL images in Fig. 2A. In addition, PL spectra in 2D-TA samples showed a dominant emission peak corresponding to $n = 1$, whereas a PL emission associated with a higher dimensionality of $n = 2$ is more pronounced in 2D-RT samples (see Fig. 2B), in accordance with GIWAXS and TEM results.

The energy-level diagrams of [2-(9H-carbazol-9-yl)ethyl]phosphonic-acid (2PACz) anchored on indium tin oxide (ITO), which we used as the hole-selective contact (22), perovskites, and C_{60} are shown in Fig. 2C. With the OLAI post-treatment, the secondary electron cut-off (E_{cutoff}) shifted to a higher binding energy, indicating that the ion-exchange-induced 3D-to-2D perovskite phase transition could lower the Fermi level (E_F) of post-treated perovskite films (figure S6). Notably, the energetic gap between E_F and the valence band maximum (VBM) of the 2D–RT sample was wider, indicating the enhanced n-type character of post-treated 3D-perovskite films that we

attributed to a successful 2D-perovskite passivation strategy (*19*). The VBM of 2D–RT films was also closer to the conduction band minimum (CBM) of C_{60} at the *n*-type contact, which resulted in more efficient charge transfer at the 2D/3D perovskite interface and the C_{60} electron-selective layer. In contrast, the CBM of 2D–TA films was much higher than the CBM of C_{60} with less *n*-type character and resulted in less efficient charge transfer of this 2D/3D perovskite interface at the electron-selective contact. In addition, the effects of 2D-perovskite capping layers also enhanced the resilience against moisture of 3D-perovskite films, as shown by contact angle measurement in figure S7.

Next, we fabricated inverted PSCs with a structure of glass/ITO/2PACz/3D-perovskite/2D-perovskite/C_{60}/BCP/Ag (Fig. 3A); Fig. 3B shows the false-colored cross-sectional SEM view of these devices. As shown in the current density-voltage (*J-V*) characteristics of the devices in Fig. 3C, the 2D–RT devices demonstrated substantially improved PCEs with a maximum PCE of 24.3% and stabilized PCE of ~24% (open-circuit voltage, V_{OC}, of ~1.20 V and fill factor, FF, of ~82%, figure S8, A and C). These results represent an absolute ~2% PCE gain upon 2D–RT passivation, and can be compared with PCEs for other inverted PSCs (see figure S9A).

Also, 2D–RT passivation enables to minimize the device energy loss ($E_{loss} = E_g – qV_{OC}$; where *q* is electron charge and E_g is the optical bandgap) up to 0.34 eV, which represents ~96% of the thermodynamic limit of the V_{OC} (1.262 V) for E_g of 1.55 eV (figure S8, D-E). The reduced non-radiative loss in 2D–RT-based devices is comparable with state-of-the-art GaAs solar cells (V_{OC} of 1.127 V, yielding ~98% of the thermodynamic limit of the V_{OC}) (*29*). The 2D-TA passivated devices suffered from lower FF values (<79%, figures S8B and S10), indicative of an energy level mismatch at the electron-selective contact, as derived from ultraviolet photoelectron spectroscopy (UPS) results (*20*). The narrow statistical distribution of the PCE, V_{OC}, FF, and short-circuit current density, J_{SC}, values of the devices are shown in figures S8B and S11, confirmed the high reproducibility of our approach. We also confirmed the effectiveness of our approaches by showing less than 0.5% deviation for person-to-person variations of seven different researchers (figure S12A).

Further, we demonstrated that our proposed passivation approach was universal for various perovskite compositions (various bandgaps) and deposition techniques (such as, one-step, two-step, and blade-coating), as demonstrated by the systematic absolute PCE enhancement of 1.5 to 2.0% of device performances in figure S12B. The reduced trap-assisted recombination of 2D/3D perovskite heterojunction devices was also investigated with transient photovoltage decay and light intensity dependent under open-circuit conditions (figure S13). The 2D-passivated devices exhibited a longer charge recombination lifetime and lower ideality factor than control devices, confirming the reduced trap-assisted recombination at 3D/C_{60} interfaces by the 2D-passivation.

Finally, we subjected our 2D-perovskite passivation-treated PSCs to a set of rigorous stability tests. First, we evaluated the stability of our encapsulated devices when subjected to industry-relevant damp-heat tests (figure S14). Here, our 2D-perovskite passivation simultaneously served as ion-migration-blocking, moisture-oxygen ingress barriers, and defect passivation layers, particularly at elevated operating temperatures (see figure S15) (*3, 14-17*). Indeed, the 2D–RT-based device retained >95% of the initial PCE (T_{95}) after >1200 hours for champion stability cells (Fig. 3D). Remarkably, after the damp-heat test, three devices showed an average PCE of 19.3 +/- 0.69%.

Our results represent the successful encapsulation of PSCs passing industry-relevant damp-heat test according to the IEC 61215:2016 protocols (*1, 2*). Also, our final PCE >19% after >1000 hours

of damp-heat test, represents a very high retained PCE (figure S9B and tabulated in table S1). There was no substantial change in the structural and optical properties of the 2D-perovskite passivation films (both 3D and 2D perovskites) after >500 hours thermal annealed at 85°C, confirming the robustness of our 2D-perovskite passivation approach (figure S16).

Note that our encapsulated devices used for stability tests exhibited slightly lower initial PCEs than the unencapsulated devices cause by J_{SC} losses originated from the encapsulant and glass sheets (figure S17). We also tested unencapsulated devices in our damp-heat chamber, and applied thermal tests in ambient air with RH was >50% (see figures S18 and S19), representative for extreme outdoor conditions. Our 2D-capping layer introduced a substantially enhanced resistance of the devices against high moisture and thermal stress. Finally, we performed maximum power point tracking (MPPT) measurements for encapsulated cells under simulated 1-sun illumination in ambient air for >500 hours (Fig. 3E, ISOS-L1). Here, the 2D–RT-based devices retained up to ~95% of their initial PCE after an MPPT test of >500 hours, whereas the control devices retained their PCE <90% for only ~100 hours.

Reference and Notes

1. A. Mei, Y. Sheng, Y. Ming, Y. Hu, Y. Rong, W. Zhang, S. Luo, G. Na, C. Tian, X. Hou, Y. Xiong, Z. Zhang, S. Liu, S. Uchida, T.-W. Kim, Y. Yuan, L. Zhang, Y. Zhou, H. Han, Stabilizing perovskite solar cells to IEC61215:2016 standards with over 9,000-h operational tracking. *Joule* **4**, 2646-2660.(2020). DOI:10.1016/j.joule.2020.09.010

2. L. Shi, M. P. Bucknall, T. L. Young, M. Zhang, L. Hu, J. Bing, D. S. Lee, J. Kim, T. Wu, N. Takamure, D. R. McKenzie, S. Huang, M. A. Green, A. W. Y. Ho-Baillie, Gas chromatography–mass spectrometry analyses of encapsulated stable perovskite solar cells. *Science* **368**, eaba2412 (2020). DOI:10.1126/science.aba2412

3. Y.-W. Jang, S. Lee, K. M. Yeom, K. Jeong, K. Choi, M. Choi, J. H. Noh, Intact 2D/3D halide junction perovskite solar cells via solid-phase in-plane growth. *Nat. Energy* **6**, 63-71 (2021). DOI:10.1038/s41560-020-00749-7

4. K. T. Cho, G. Grancini, Yo. Lee, E. Oveisi, J. Ryu, O. Almora, M. Tschumi, P. A. Schouwink, G. Seo, S. Heo, J. Park, J. Jang, Sa. Paek, G. G.-Belmonte, M. K. Nazeeruddin, Selective growth of layered perovskite for stable and efficient photovoltaics. *Energy Environ. Sci.* **11**, 952-959 (2018). DOI: 10.1039/C7EE03513F

5. S. Yang, S. Chen, E. Mosconi, Y. Fang, X. Xiao, C. Wang, Y. Zhou, Z. Yu, J. Zhao, Y. Gao, F. D. Angelis, J. Huang, Stabilizing halide perovskite surfaces for solar cell operation with wide-bandgap lead oxysalts. *Science* **365**, 473-478 (2019). DOI:10.1126/science.aax3294

6. Y. Lin, Y. Bai, Y. Fang, Z. Chen, S. Yang, X. Zheng, S. Tang, Y. Liu, J. Zhao, J. Huang, Enhanced thermal stability in perovskite solar cells by assembling 2D/3D stacking structures. *J. Phy. Chem. Lett.* **9**, 654-658 (2018). DOI:10.1021/acs.jpclett.7b02679

7. Y.-H. Lin, N. Sakai, P. Da, J. Wu, H. C. Sansom, A. J. Ramadan, S.Mahesh, J. Liu, Robert D. J. Oliver, J. Lim, L. Aspitarte, K. Sharma, P. K. Madhu, A. B. M.-Vilches, P. K. Nayak, S. Bai, F. Gao, C. R. M. Grovenor, M. B. Johnston, J. G. Labram, J. R. Durrant, J. M. Ball, B. Wenger, B. Stannowski, H. J. Snaith, A piperidinium salt stabilizes efficient metal-halide perovskite solar cells. *Science* **369**, (2020). DOI: 10.1126/science.aba1628

8. J. Xu, C. C. Boyd, Z. J. Yu, A. F. Palmstrom, D. J. Witter, B. W. Larson, R. M. France, J. Werner, S. P. Harvey, E. J. Wolf, W. Weigand, S. Manzoor, M. F. A. M. v. Hest, J. J. Berry, J. M. Luther, Z. C. Holman, M. D. McGehee, Triple-halide wide-band gap

perovskites with suppressed phase segregation for efficient tandems. *Science* **367**, 1097-1104 (2020). DOI:10.1126/science.aaz5074

9. Y. Zhao, P. Miao, J. Elia, H. Hu, X. Wang, T. Heumueller, Y. Hou, G. J. Matt, A. Osvet, Y.-T. Chen, M. Tarragó, D. de Ligny, T. Przybilla, P. Denninger, J. Will, J. Zhang, X. Tang, N. Li, C. He, A. Pan, A. J. Meixner, E. Spiecker, D. Zhang, C. J. Brabec, Strain-activated light-induced halide segregation in mixed-halide perovskite solids. *Nat. Commun.* **11**, 6328 (2020). DOI:10.1038/s41467-020-20066-7

10. J. Jeong, M. Kim, J. Seo, H. Lu, P. Ahlawat, A. Mishra, Y. Yang, M. A. Hope, F. T. Eickemeyer, M. Kim, Y. J. Yoon, I. W. Choi, B. P. Darwich, S. J. Choi, Y. Jo, J. H. Lee, B. Walker, S. M. Zakeeruddin, L. Emsley, U. Rothlisberger, A. Hagfeldt, D. S. Kim, M. Grätzel, J. Y. Kim, Pseudo-halide anion engineering for α-FAPbI$_3$ perovskite solar cells. *Nature* **592**, 381-385 (2021). DOI:10.1038/s41586-021-03406-5

11. S. Chen, X. Dai, S. Xu, H. Jiao, L. Zhao, J. Huang, Stabilizing perovskite-substrate interfaces for high-performance perovskite modules. *Science* **373**, 902-907 (2021). DOI:10.1126/science.abi6323

12. R. Wang, J. Xue, K.-L. Wang, Z.-K. Wang, Y. Luo, D. Fenning, G. Xu, S. Nuryyeva, T. Huang, Y. Zhao, J. L. Yang, J. Zhu, M. Wang, S. Tan, I. Yavuz, K. N. Houk, Y. Yang, Constructive molecular configurations for surface-defect passivation of perovskite photovoltaics. *Science* **366**, 1509-1513 (2019). DOI:10.1126/science.aay9698

13. H. Zhou, Q. Chen, G. Li, S. Luo, T.-b. Song, H.-S. Duan, Z. Hong, J. You, Y. Liu, Y. Yang, Interface engineering of highly efficient perovskite solar cells. *Science* **345**, 542-546 (2014). DOI:10.1126/science.1254050

14. J.J. Yoo, S. Wieghold, M. C. Sponseller, M. R. Chua, S. N. Bertram, N. T. P. Hartono, J. S. Tresback, E. C. Hansen, J.-P. Corea-Baena, V. Bulovic´, T. Buonassisi, S. S. Shin, M. G. Bawendi, An interface stabilized perovskite solar cell with high stabilized efficiency and low voltage loss. *Energy Environ. Sci.* **12**, 2192-2199 (2019). DOI: 10.1039/c9ee00751b

15. E. H. Jung, N. J. Jeon, E. Y. Park, C. S. Moon, T. J. Shin, T.-Y. Yang, J. H. Noh, J. Seo, Efficient, stable and scalable perovskite solar cells using poly(3-hexylthiophene). *Nature* **567**, 511-515 (2019). DOI:10.1038/s41586-019-1036-3

16. A. H. Proppe, A. Johnston, S. Teale, A. Mahata, R. Quintero-Bermudez, E. H. Jung, L. Grater, T. Cui, T. Filleter, C.-Y. Kim, S. O. Kelley, F. De Angelis, E. H. Sargent, Multication perovskite 2D/3D interfaces form via progressive dimensional reduction. *Nat. Commun.* **12**, 3472 (2021). DOI:10.1038/s41467-021-23616-9

17. G. Yang, Z. Ren, K. Liu, M. Qin, W. Deng, H. Zhang, H. Wang, J. Liang, F. Ye, Q. Liang, H. Yin, Y. Chen, Y. Zhuang, S. Li, B. Gao, J. Wang, T. Shi, X. Wang, X. Lu, H. Wu, J. Hou, D. Lei, S. K. So, Y. Yang, G. Fang, G. Li, Stable and low-photovoltage-loss perovskite solar cells by multifunctional passivation. *Nat. Photon.* **15**, 681-689 (2021). DOI:10.1038/s41566-021-00829-4

18. Q. Yao, Q. Xue, Z. Li, K. Zhang, T. Zhang, N. Li, S. Yang, C. J. Brabec, H.-L. Yip, Y. Cao, Graded 2D/3D perovskite heterostructure for efficient and operationally stable MA-free perovskite solar cells. *Adv. Mater.* **32**, 2000571 (2020). DOI:10.1002/adma.202000571

19. D. H. Cao, C. C. Stoumpos, O. K. Farha, J. T. Hupp, M. G. Kanatzidis, 2D homologous perovskites as light-absorbing materials for solar cell applications. *J. Am. Chem. Soc.* **137**, 7843-7850 (2015). DOI:10.1021/jacs.5b03796

20. J. Yang, S. Xiong, J. Song, H. Wu, Y. Zeng, L. Lu, K. Shen, T. Hao, Z. Ma, F. Liu, C. Duan, M. Fahlman, Q. Bao, Energetics and energy loss in 2D ruddlesden–popper perovskite solar cells. *Adv. Energy Mater.* **10**, 2000687 (2020). DOI: 10.1002/aenm.202000687

21. Y. Shao, Z. Xiao, C. Bi, Y. Yuan, J. Huang, Origin and elimination of photocurrent hysteresis by fullerene passivation in $CH_3NH_3PbI_3$ planar heterojunction solar cells. *Nat. Commun.* **5**, 5784 (2014). DOI:10.1038/ncomms6784

22. A. Al-Ashouri, A. Magomedov, M. Roß, M. Jošt, M. Talaikis, G. Chistiakova, T. Bertram, J. A. Márquez, E. Köhnen, E. Kasparavičius, S. Levcenco, L. Gil-Escrig, C. J. Hages, R. Schlatmann, B. Rech, T. Malinauskas, T. Unold, C. A. Kaufmann, L. Korte, G. Niaura, V. Getautis, S. Albrecht, Conformal monolayer contacts with lossless interfaces for perovskite single junction and monolithic tandem solar cells. *Energy Environ. Sci.* **12**, 3356-3369 (2019). DOI:10.1039/C9EE02268F

23. A. Al-Ashouri, E. Köhnen, B. Li, A. Magomedov, H. Hempel, P. Caprioglio, J. A. Márquez, A. B. M. Vilches, E. Kasparavicius, J. A. Smith, N. Phung, D. Menzel, M. Grischek, L. Kegelmann, D. Skroblin, C. Gollwitzer, T. Malinauskas, M. Jošt, G. Matič, B. Rech, R. Schlatmann, M. Topič, L. Korte, A. Abate, B. Stannowski, D. Neher, M. Stolterfoht, T. Unold, V. Getautis, S. Albrecht, Monolithic perovskite/silicon tandem solar cell with >29% efficiency by enhanced hole extraction. *Science* **370**, 1300-1309 (2020). DOI:10.1126/science.abd4016

24. E. Aktas, N. Phung, H. Köbler, D. A. González, M. Méndez, I. Kafedjiska, S.-H. Turren-Cruz, R. Wenisch, I. Lauermann, A. Abate, E. Palomares, Understanding the perovskite/self-assembled selective contact interface for ultra-stable and highly efficient p–i–n perovskite solar cells. *Energy Environ. Sci.* **14**, 3976-3985 (2021). DOI:10.1039/D0EE03807E

25. I. Levine, A. Al-Ashouri, A. Musiienko, H. Hempel, A. Magomedov, A. Drevilkauskaite, V. Getautis, D. Menzel, K. Hinrichs, T. Unold, S. Albrecht, T. Dittrich, Charge transfer rates and electron trapping at buried interfaces of perovskite solar cells. *Joule* **5**, 2915-2933 (2021). DOI: 10.1016/j.joule.2021.07.016

26. S. Gharibzadeh, P. Fassl, I. M. Hossain, P. Rohrbeck, M. Frericks, M. Schmidt, T. Duong, M. R. Khan, T. Abzieher, B. A. Nejand, F. Schackmar, O. Almora, T. Feeney, R. Singh, D. Fuchs, U. Lemmer, J. P. Hofmann, S. A. L. Weber, U. W. Paetzold, Two birds with one stone: dual grain-boundary and interface passivation enables >22% efficient inverted methylammonium-free perovskite solar cells. *Energy Environ. Sci.* **14**, 5875-5893 (2021). DOI:10.1039/D1EE01508G

27. J. Xing, Y. Zhao, M. Askerka, L. N. Quan, X. Gong, W. Zhao, J. Zhao, H. Tan, G. Long, L. Gao, Z. Yang, O. Voznyy, J. Tang, Z.-H. Lu, Q. Xiong, E. H. Sargent, Color-stable highly luminescent sky-blue perovskite light-emitting diodes. *Nat. Commun.* **9**, 3541 (2018). DOI:10.1038/s41467-018-05909-8

28. A. H. Proppe, M. Wei, B. Chen, R. Quintero-Bermudez, S. O. Kelley, E. H. Sargent, Photochemically cross-linked quantum well ligands for 2D/3D perovskite photovoltaics with improved photovoltage and stability. *J. Am. Chem. Soc.* **141**, 14180-14189 (2019). DOI:10.1021/jacs.9b05083

29. M. A. Green, E. D. Dunlop, D. H. Levi, J. Hohl-Ebinger, M. Yoshita, A. W. Y. Ho-Baillie, Solar cell efficiency tables (ver. 53). *Prog. Photovolt. Res. Appl.* **27**, 3-12 (2018). DOI:10.1002/pip.3102

30. E. Aydin, J. Liu, Es. Ugur, R. Azmi, G. T. Harrison, Y. Hou, Bi. Chen, S. Zhumagali, M. D. Bastiani, M. Wang, W. Raja, T. G Allen, A. U. Rehman, A. S. Subbiah, M. Babics, A. Babayigit, F. H. Isikgor, K. Wang, E. V. Kerschaver, L. Tsetseris, E. H. Sargent, F. Laquai, S. D. Wolf, Ligand-bridged charge extraction and enhanced quantum efficiency enable efficient n–i–p perovskite/silicon tandem solar cells. *Energy Environ. Sci.* **8**, 4377-4390 (2021). DOI.org/10.1039/D1EE01206A

31. R. Azmi, N. Nurrosyid, S.-H. Lee, M. A. Mubarok, W. Lee, S. Hwang, W. Yin, T. K. Ahn, T.-W. Kim, D. Y. Ryu, Y. R. Do, S.-Y. Jang, Shallow and deep trap state passivation for low-temperature processed perovskite solar cells. *ACS Energy Lett.* **5**, 1396-1403 (2020). DOI.org/10.1021/acsenergylett.0c00596

32. R. Azmi, C.-L. Lee, I. H. Jung, S.-Y. Jang, Simultaneous improvement in efficiency and stability of low-temperature-processed perovskite solar cells by interfacial control. *Adv. Energy Mater.* **8**, 1702934 (2018). DOI.org/10.1002/aenm.201702934

33. G. Kresse, D. Joubert, From ultrasoft pseudopotentials to the projector augmented-wave method. *Phys. Rev. B* **59**, 1758-1775 (1999). DOI:10.1103/PhysRevB.59.1758

34. S. Wang, W.-b. Xiao, F. Wang, Structural, electronic, and optical properties of cubic formamidinium lead iodide perovskite: a first-principles investigation. *RSC Adv.* **10**, 32364-32369 (2020). DOI:10.1039/D0RA06028C

35. J. H. Heo, Y. K. Choi, C. W. Koh, H. Y. Woo, S. H. Im, Semitransparent $FAPbI_{3-x}Br_x$ perovskite solar cells stable under simultaneous damp heat (85 °C/85%) and 1 sun light soaking. *Adv. Mater. Tech.* **4**, 1800390 (2019). DOI:10.1002/admt.201800390

36. T. Matsui, T. Yamamoto, T. Nishihara, R. Morisawa, T. Yokoyama, T. Sekiguchi, T. Negami, Compositional engineering for thermally stable, highly efficient perovskite solar cells exceeding 20% power conversion efficiency with 85 °C/85% 1000 h stability. *Adv. Mater.* **31**, 1806823 (2019). DOI:10.1002/adma.201806823

37. J. Peng, D. Walter, Y. Ren, M. Tebyetekerwa, Y. Wu, T. Duong, Q. Lin, J. Li, T. Lu, M.A. Mahmud, O. L. C. Lem, W. L. S. Zhao, Y. Liu, H. Shen, L. Li, F. Kremer, H. T. Nguyen, D.-Y. Choi, K. J. Weber, K. R. Catchpole, T. P. White, Nanoscale localized contacts for high fill factors in polymer-passivated perovskite solar cells. *Science* **371**, 390-395 (2021). DOI: 10.1126/science.abb8687

38. K. A. Bush, A. F. Palmstrom, Z. J. Yu, M. Boccard, R. Cheacharoen, J. P. Mailoa, D. P. McMeekin, R. L. Z. Hoye, C. D. Bailie, T. Leijtens, I. M. Peters, M. C. Minichetti, N. Rolston, R. Prasanna, S. Sofia, D. Harwood, W. Ma, F. Moghadam, H. J. Snaith, T. Buonassisi, Z. C. Holman, S. F. Bent, M. D. McGehee, 23.6%-efficient monolithic perovskite/silicon tandem solar cells with improved stability. *Nat. Energy* **2**, 17009 (2017). DOI:10.1038/nenergy.2017.9

Data and materials availability: All data are available in the main text or the supplementary material.

SUPPLEMENTARY MATERIALS

Materials and Methods

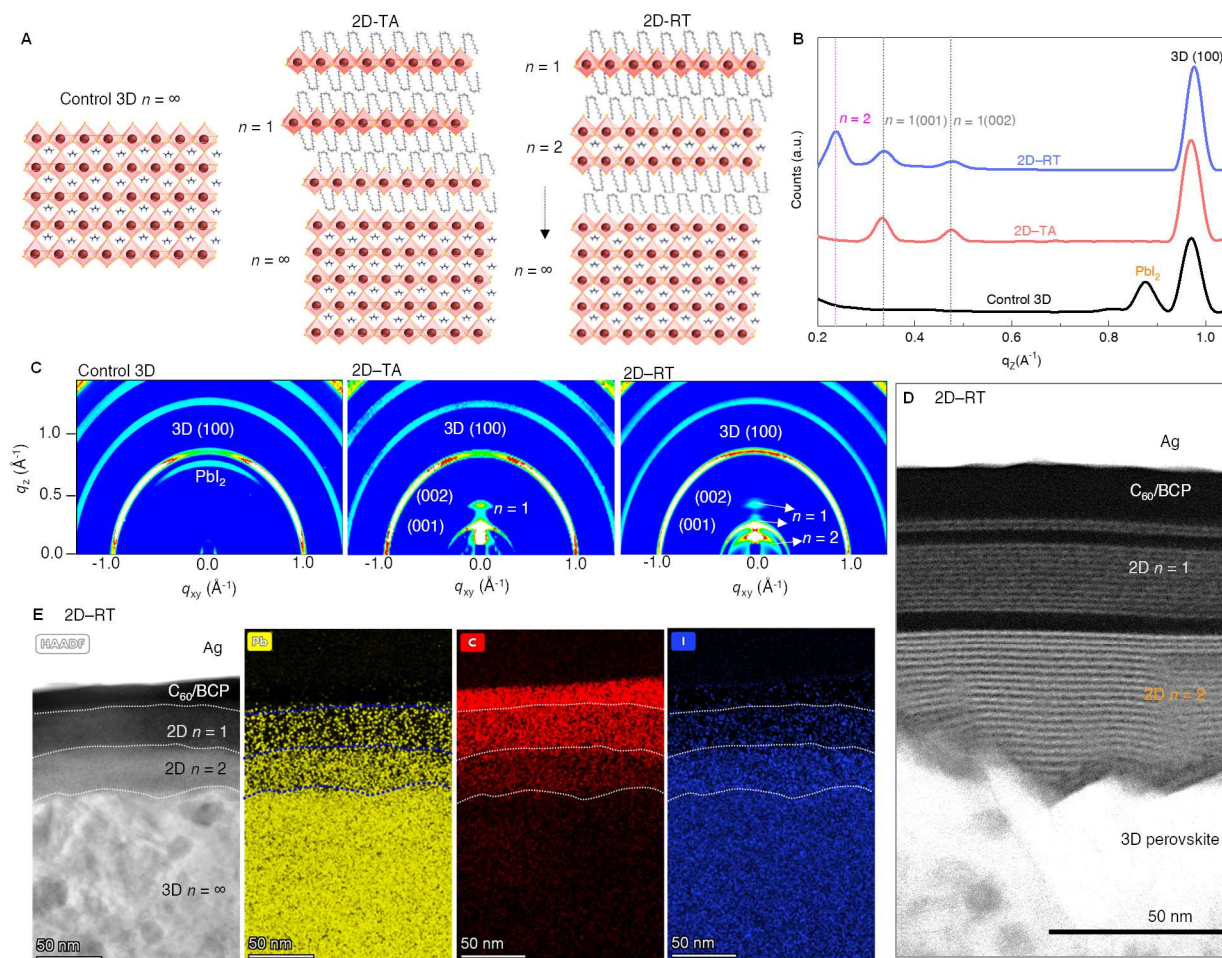Figs. S1 to S19

Table S1

References (*30–38*)

FIG. 1. Structure of 2D perovskite dimensionality control by tuning the annealing conditions. **(A)** Schematic illustration of 2D perovskite passivation with different *n* layers under thermal annealing at 100 °C and room-temperature process. **(B)** Integrated intensity of GIWAXS data along q$_z$. **(C)** GIWAXS maps of each film. **(D)** Cross-sectional HR-STEM image and **(E)** energy-dispersive x-ray spectroscopy elemental map of the cross-sectional STEM image of the 2D-RT samples.
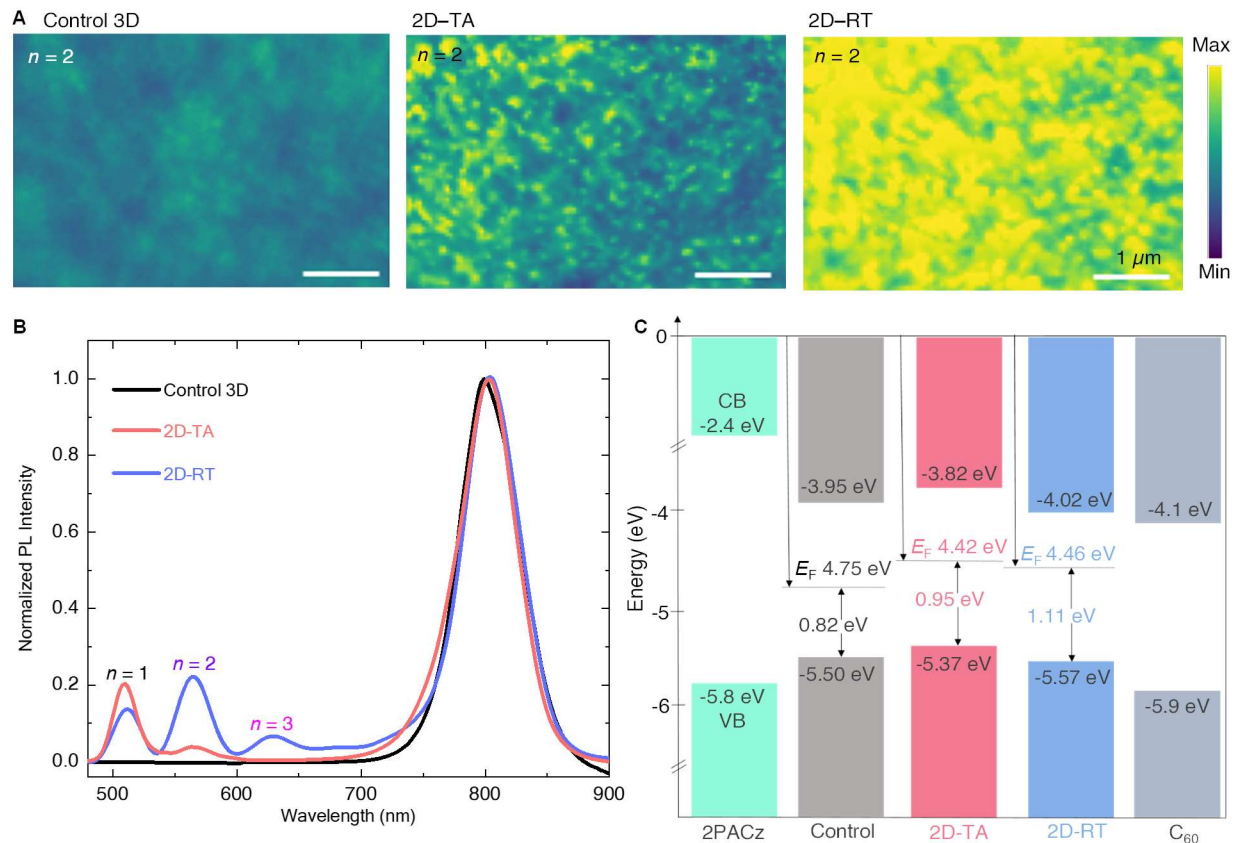
FIG. 2. Optical characterization and energetic alignments of perovskite films with and without 2D perovskite passivation. **(A)** PL images of control and OLAI treated films perovskite thin films at wavelength ~570 nm, which corresponds to $n = 2$ layers (images extracted using PHySpecV2). **(B)** Normalized PL spectra of each film from low to high wavelengths. **(C)** Energy level scheme for the control and OLAI treated films extracted from UPS data. The VBM was obtained as $h\nu - (E_{cutoff} - E_{VB, min})$. The position of the CBM with respect to the VBM was defined by optical-E_g (1.55 eV).

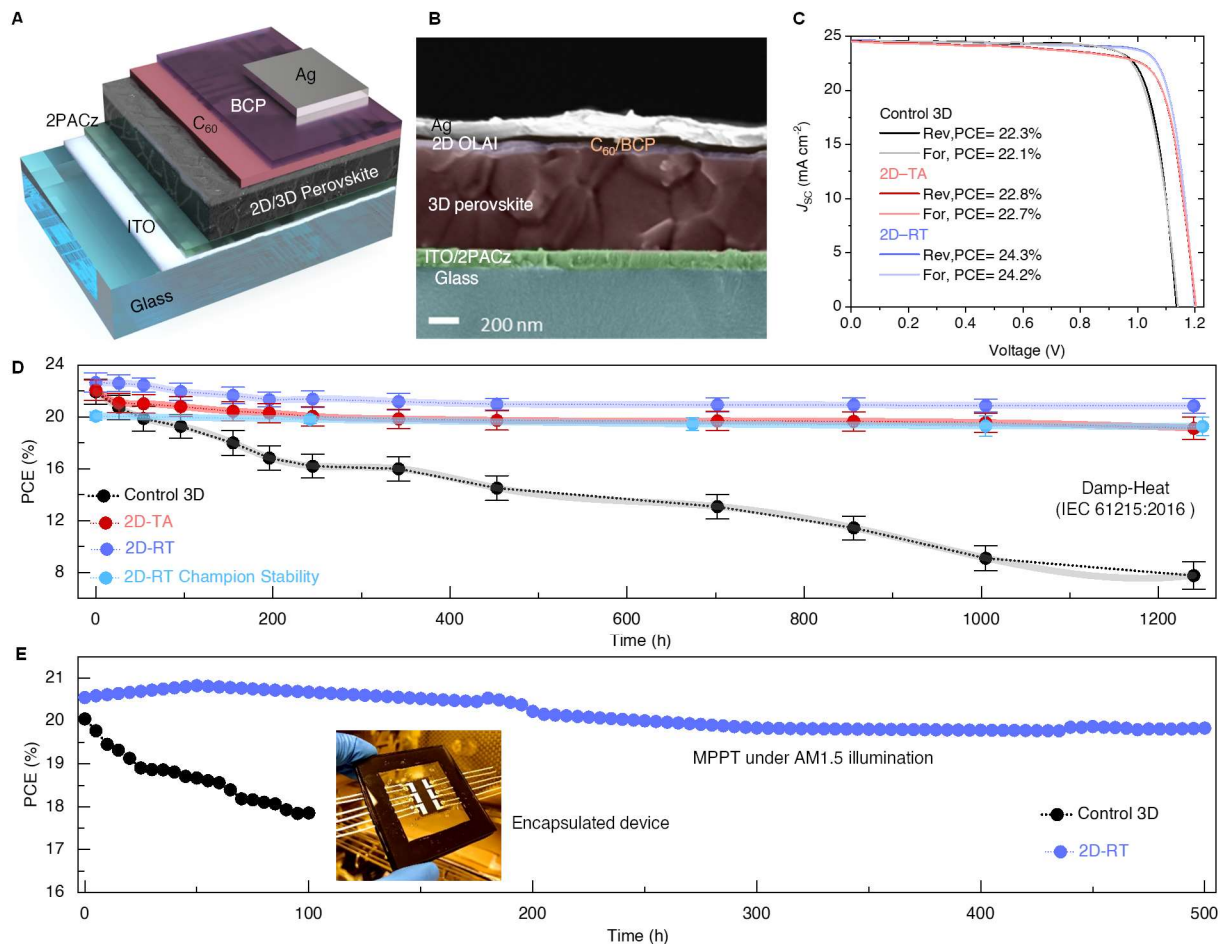**FIG. 3. Device performance and stability of 2D/3D perovskite heterojunction**. **(A)** Device architecture of inverted PSCs. **(B)** Cross-sectional SEM image of inverted cells. **(C)** *J–V* scan of champion PSCs. **(D)** Variation of the PCEs at damp-heat test of encapsulated devices. The continuous lines are guides to eye. **(E)** Continuous MPP tracking for the encapsulated control and 2D–RT cells under AM 1.5 illumination in ambient air. The inset figure is the photograph of the encapsulated device.

Science

▨AAAS

Supplementary Materials for

Damp-heat stable perovskite solar cells with tailored dimensionality 2D/3D heterojunctions

Randi Azmi[1], Esma Ugur[1], Akmaral Seitkhan[1], Faisal Aljamaan[1], Anand S. Subbiah[1], Jiang Liu[1], George T. Harisson[1], Mohamad I. Nugraha[1], Mathan K. Eswaran[1], Maxime Babics[1], Yuan Chen[2], Fuzong Xu[1], Thomas G. Allen[1], Atteq ur Rehman[1], Chien-Lung Wang[2], Thomas D. Anthopoulos[1], Udo Schwingenschlögl[1], Michele De Bastiani[1], Erkan Aydin[1], Stefaan De Wolf[1]*

Correspondence to: stefaan.dewolf@kaust.edu.sa

This PDF file includes:

Materials and Methods

Materials

[2-(9H-Carbazol-9-yl)ethyl]phosphonic acid (2PACz, >98.0% purity) was purchased from TCI. The dimethylformamide (DMF), dimethylsulfoxide (DMSO), dimethyl propylene urea (DMPU) and chloroform were all purchased from Sigma Aldrich. Formamidium iodide (FAI), methyl-ammonium iodide (MAI), and cesium iodide (CsI) were purchased from Greatcellsolar. Olaylammonium iodide (OLAI) and methyl-ammonium chloride (MACl) were purchased from Xi'an Polymer L.T. Lead (II) iodide (PbI_2 ultra-dry, 99.9% purity) was purchased from Alfa Aesar. C_{60} (>99.5% purity) and bathocuproine (BCP, >99% purity) were purchased from Ossila Ltd. Thermal polyurethane (TPU) was purchased from Schweitzer-Mauduit International (SWM). Butyl rubber edge sealant (HelioSeal PVS 101) was purchased from Kömerling Chemische Fabrik GMBH. All materials were directly used without purification.

Device fabrication

ITO glass was sequentially cleaned with acetone and isopropyl alcohol (IPA) for 15 min, respectively. Before use, the ITO/glass substrates were cleaned with ultraviolet ozone for 15 min. Then, the ITO/glass substrates were spin-coated with a thin layer of a self-assembled monolayer (SAM) 2PACz ([2-(9H-carbazol-9-yl)ethyl]phosphonic acid) at 5,000 r.p.m. for 30 s followed by annealing at 100 °C for 10 min (0.5-1.0 mg/mL in ethanol). After cooling down, the 2PACz films were then washed by ethanol by dynamic coating at 5,000 r.p.m. for 30 s to remove unbounded molecules, followed by additional annealing at 100 °C for 5 min.

Perovskite $Cs_{0.03}(FA_{0.90}MA_{0.10})_{0.97}PbI_3$ layers

A mixture of perovskite solution (1.5 M) composed of mixed cations (PbI_2: 691.5 mg, CsI: 11.7 mg, FAI: 225.1 mg, and MAI: 15.4 mg with 30 mol% of MACl) was dissolved in a mixed solvent (DMF/DMSO with 4/1 vol. ratio) according to a formula of $Cs_{0.03}(FA_{0.90}MA_{0.10})_{0.97}PbI_3$. A two-step spin-coating procedure with 2,000 r.p.m. for 40 s and 6,000 r.p.m. for 10 s was adopted to prepare perovskite films. Anisole (300 µl) was dropped on the spinning substrate during the last 10 s of the second spin-coating step. Subsequently, the sample was annealed at 100 °C for 30 min. After cooling down, the 2D passivation by solution post-treatment was carried. Typically, OLAI molecules were dissolved in chloroform with concentrations ranging from 0.5 to 2.5 mg/mL. Then, 2D ligand solution (100 µL) was spin-coated onto the as-prepared perovskite films at 5,000 r.p.m. for 25 s. It should be noted, the temperature of N_2 glove box was recorded around 25 °C during 2D passivation (the digital thermometer was placed near by spin-coater). Then the treated perovskite films were annealed at 100 °C for 10 min for 2D-TA-based samples; and stored overnight at room-temperature (under dark and inside N_2 glovebox with O_2 level was <10 ppm and H_2O level was <0.1 ppm) for 2D-RT-based samples. After Annealed or stored overnight, the treated films with 2D perovskite passivation were then washed one time with chloroform at 5,000 r.p.m. for 20 s to remove unbounded 2D ligands. All procedures were done in an N_2 glove box.

Perovskite $Cs_{0.05}FA_{0.80}MA_{0.15}PbI_{2.25}Br_{0.75}$ layers

For wide-bandgap perovskite, a mixture of perovskite solution (1.4 M) composed of mixed cations (PbI_2: 568.2 mg, $PbBr_2$: 61.3, CsI: 18.2 mg, FAI: 192.6 mg, and MABr: 23.5 mg with 15 mol% of MACl) was dissolved in a mixed solvent (DMF/DMSO with 4/1 ratio) according to a formula of $Cs_{0.05}FA_{0.80}MA_{0.15}PbI_{2.25}Br_{0.75}$.(30) A two-step spin-coating procedure with 2,000 r.p.m. for 40 s and 6,000 r.p.m. for 10 s was adopted to prepare perovskite film. Anisole (300 µL) was dropped on

the spinning substrate during the last 10 s of the second spin-coating step. Subsequently, the sample was annealed at 100 °C for 15 min. For fabricating blade-coated devices, PTAA (2 mg/mL in chlorobenzene) solution is spin-coated (5,000 r.p.m. for 30s) and annealed at 100 °C for 10 mins. The perovskite absorber layer is deposited on top of the HTL, by employing a 1.5 M solution of $Cs_{0.15}(FA_{0.85}MA_{0.15})_{0.85}PbI_{0.7}Br_{0.3}$ in DMF solution. 25 µL of DMPU and 18 mg of MACl were introduced as additives for 1 ml of precursor solution. The substrates were blade-coated using 10 µL of the precursor solution at room-temperature at a speed of 15 mm/s. The blade-substrate gap was kept at 100 µm and a laminar flow air gun was used to induce crystallization of the precursor thin film. The films were then annealed at 70 °C for 10 min and 100 °C for 30 min, subsequently. The 2D passivation was done as described above.

Perovskite $FAMAPbI_3$ and $MAPbI_3$ layers (two-step method)
The two-step inter-diffusion method was used to prepare double cation $FAMAPbI_3$- and $MAPbI_3$-based perovskite films on ITO/2PACz substrates, with modification from previous report.(31,32) A mixture solution of 1.5 M PbI_2 in DMF/DMSO (9/1, v/v) solvent with 0.5 mol% of potassium iodide was stirred and heated at 75°C prior to use. Then, the solution was spin-coated at 2,500 r.p.m. for 30 s followed by annealing at 70°C for 1 min. After cooling to RT, mixed solution of 0.5 M FAI/MAI (0.7/0.3, molar ratio with or without 0.15 M of MACl) in IPA or 0.5 M MAI in IPA were dropped onto the PbI_2 layers for preparing $FAMAPbI_3$ and $MAPbI_3$ perovskites, respectively. Then, the films were annealed at 80°C for 1 min. After cooling, the perovskite films were washed with IPA via drop-casting at 4,000 r.p.m. for 20 s, followed by thermal annealing at 120 °C for 20 min. The 2D passivation was done as described above.

After the perovskite deposition, samples were transferred into a thermal evaporator for the C_{60} (25 nm) and BCP (5 nm) deposition. For the final step, a 120 nm thick Ag layer was evaporated at low pressure ($< 10^{-6}$ Torr) with an area of ~0.1 cm^2. For *J-V* measurements, a black metal mask with an aperture area of 0.0715 cm^2 was used to define the active area of the devices accurately. A ~120 nm MgF_2 was also evaporated at the glass side to minimize the reflection losses from the glass substrates.

Perovskite film characterizations
The photo-emission spectra of the encapsulated perovskite thin films were collected using a hyperspectral imaging system coupled to a microscope with 2 nm spectral resolution (Photon etc., IMA). The samples were excited with a 405 nm laser where the excitation was incident on the top surface of the perovskite films. All Grazing-Incidence Wide-Angle X-ray Scattering (GIWAXS) patterns of samples were acquired at the BL17A1 beamline in the National Synchrotron Radiation Research Center (NSRRC), Taiwan. A Mar345 image plate detector was used to capture the scattering patterns. The sample-to-detector distance is 315.6 mm, which was calibrated from the AgBe standard. The wavelength of the incident X-rays is 1.32 Å. Typical GIWAXS patterns were obtained from an incidence angle of 0.20° to 1.00°. For the cross-sectional TEM measurements, the lamella was prepared first in a scanning electron microscope (Helios G4 DualBeam, FEI), equipped with an EasyLift nanomanipulator with the help of a Ga focused ion beam (FIB). To protect the sample, the protective carbon and platinum layers were deposited under electron and ion beams. The bulk of the sample was milled with the ion beam (30 kV, 20 nA), and attached to the TEM copper grid in accordance with the lift-out method. The lamella was thinned down with the FIB gradually decreasing the current (30 kV, 2.8 nA – 90 pA). The final cleaning was

performed at 5 kV, 81 pA and 2 kV, 28 pA to remove any possible contamination. The imaging and elemental mapping was conducted in Titan Cs Probe TEM equipped with EDX and HAADF detector in STEM mode at 300 kV operating voltage. Unless stated otherwise, all measured perovskite films for the characterization mentioned above used higher OLAI concentrations (2 mg/mL) to help the investigation of the 2D perovskite properties.

The Bruker Dimension-Icon system atomic force microscopy (AFM) measurements were carried to investigate perovskite films' morphology. The X-ray diffraction patterns were recorded with a Bruker D2 Advance diffractometer (Bruker, PHASER) with Cu Ka radiation (l = 1.5418 A˚). Contact angles were measured with a KRUSS-The Drop Shape Analyzer DSA100 system using water as the wetting solvent. A Cary 5000 UV-vis-NIR spectrophotometer was used to measure the absorbance of perovskite films on the glass substrates. XPS, UPS, and LE-IPES characterization was carried out in an ultra-high vacuum (UHV) *ScientaOmicron* multiprobe XPS/UPS system equipped with a home-built LE-IPES setup. Samples were mounted and transferred into the system with minimal exposure (< the 30s) to air. Two separate samples were used by cutting samples, one UPS and subsequent IPES analysis and one for XPS to prevent X-ray or electron beam-induced degradation from impacting analysis. XPS utilized an Al Kα 1486.7 eV XM1000 X-ray source operating at a power of 390 W, with a Sphera II hemispherical analyzer equipped with a 7-channeletron detector. XPS scans were conducted with a 50 eV (15 eV) constant pass energy for the survey (high resolution) scans at an electron take-off angle of 0° (perpendicular to sample surface) with the sample surface in good electrical contact to the analyzer. The XPS/UPS electron analyzer work function was calibrated to an Ar+ sputter cleaned Ag foil's Ag 3d peak and Ef energy edge. UPS was acquired with a He vacuum ultraviolet (VUV) discharge lamp with a copper attenuation aperture to limit VUV intensity and surface charging. All scans were conducted with He1α (21.22 eV) excitation and a 5 eV constant pass energy at an electron take-off angle of 0°. The analysis region in both XPS and UPS is estimated to be 60μm in size. LE-IPES was conducted in the Bremsstrahlung isochromatic mode in the adjoining chamber consisting of a monoenergetic source (*Staib*) of 0.25 eV energy dispersion and drain current of 20-40 μA with a 2-3 mm sized spot, directed normal to the sample surface. The emitted IPES light was detected through a lens assembly (vacuum and airside), bandpass filter of 280 nm (4.43 eV), and solid-state photo-multiplier tube (PMT) (*Hammatsu*). Scans were conducted at a sample bias of +20V and 0 eV electron kinetic energy, and subsequent vacuum level calibration was done to the turn-on point in the drain current energy trace recorded simultaneously with the PMT signal. Spectra were interpreted without normalization to the drain current. Analysis of XPS was conducted in CASA XPS, where a Tougaard based background function was used for the inelastic background, and mixed Gaussian-Lorenzian (70:30) peaks were fitted. Analysis of UPS and IPES was made in origin fitting Gaussian functions to the VBM/CBM and linear extrapolation to identify the secondary electron cutoff (SECO). The 2D ligand concentration here followed the optimum concentration for the device's performance (0.5-1.0 mg/mL).

Device characterizations

The *J-V* characteristics were investigated using a Keithley 2400 source unit under a light intensity of AM 1.5 G (100 mW cm^{-2}) illumination with an Abet Technologies Sun 3000 solar simulator. The spectral mismatch was calibrated using a KG-5 filter-covered mono-silicon standard cell (Newport). All devices were measured for the reverse and forward scans with a scanning rate of 0.1 V s^{-1}. The external quantum efficiency (EQE) spectra were obtained by passing the output of a 400 W Xenon lamp through a monochromator and filter under an N$_2$ glove box. The calibration was performed with a 603621 Calibrated Silicon and Germanium Reference Detector.

Next, the capacitance measurements were performed using an impedance spectrometer (potentiostat/galvanostat, Metrohm Autolab B.V.) with a sweeping frequency from 1 MHz to 1 Hz (10 mV AC voltage). The capacitance–voltage was monitored by varying the voltage from 0 to 1.2 V while keeping the frequency constant at 1 kHz. The transient photo-voltage (TPV), transient photo-current (TPC), and light-intensity dependent J-V measurements were performed using PAIOS 3.2(Fluxim) with white led under a maximum light intensity of 200 mW cm^{-2}. All measurements were done under an N_2–filled glove box.

Computational method

Density functional theory is used in the generalized gradient approximation of Perdew, Burke, and Ernzerhof (Vienna ab-initio simulation package;(33) projector augmented wave method; 500 eV plane wave cut-off). A $3 \times 3 \times 2$ supercell of cubic α-FAPbI$_3$ with space group Pm3m (for which a relaxed lattice constant of 6.52 Å is obtained in agreement with the literature(34) is built and is augmented with a vacuum layer of 25 Å thickness in the [001] direction to achieve a slab model of the energetically favourable PbI$_2$-terminated (001) surface. In agreement with the literature, the orientation of the FA molecules in the surface layer is found to change from horizontal to vertical.(35) The Brillouin zone is sampled on a Monkhorst-Pack $3 \times 3 \times 1$ k-mesh, the total energy is converged to 10^{-5} eV, and the maximum atomic force is converged to 0.001 eV Å^{-1}.

Device stability testing

To measure the damp-heat test of the encapsulated devices, we kept the cells at constant temperature and humidity levels (85 °C/85% of RH) in the environmental test chamber (Weisstechnik as shown in figure S14) for over 1,000 h. The encapsulated devices were measured periodically under an N_2–filled glove box after around 30 min cooling of devices in ambient air. For the stability test, ~10 nm layer of tin(IV) oxide and an 80 nm layer of indium zinc oxide were deposited on top of the C$_{60}$ sequentially, by atomic layer and sputtering depositions, respectively, to replace the BCP layer. Unless otherwise stated, a ~40 nm thick of nickel (II) oxide (using NiO target (Plasmaterials, 99.9%) and radiofrequency sputtering at room temperature in pure Ar atmosphere and base pressure of $< 10^{-6}$ Torr) with potassium chloride passivated for the champion damp-heat cells were used as holes transporting layers. The operational stability tests were carried out at the MPPT for the encapsulated devices under AM1.5 illumination (100 mW cm^{-2}) in ambient air at ~40 °C. The voltage at the MPPT was automatically applied, and the power output of the devices was tracked.

Encapsulation

For our encapsulation, we use industry-compatible materials and processes. First, ribbons (Ulbrich Solar Technologies) are soldered to the electrodes of the devices to extend the connections. The device is encapsulated between two glasses and two layers of encapsulant films. We use edge sealant (PVS 101) to prevent moisture ingress from the sides of the device. The stack is vacuum laminated in an industrial laminator (Ecolam5 Ecoprogetti) at 120°C for 20 min. All processes were done in ambient air. It should be noted that the perovskite devices are stable during the encapsulation process.
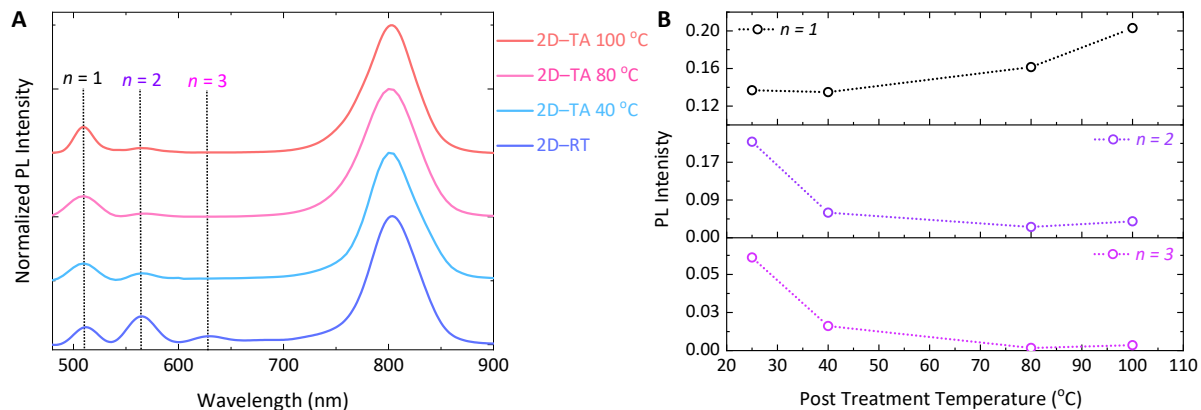
Fig. S1. (A) Normalized PL emission of 2D-passivated sample at various temperature (room temperature, 40 and 80 and 100 °C). **(B)** The evolution of PL peak intensity (extracted from panel A) plots of each $n = 1, 2$ and 3 for various annealing temperatures. Thermal annealing of 2D perovskite is for 10 min as described in experimental method. All 2D-TA samples show a dominant peak at ~510 nm which correspond to $n = 1$ peak, while higher-dimensionality ($n \geq 2$) becomes more pronounced by decreasing temperature annealing process.
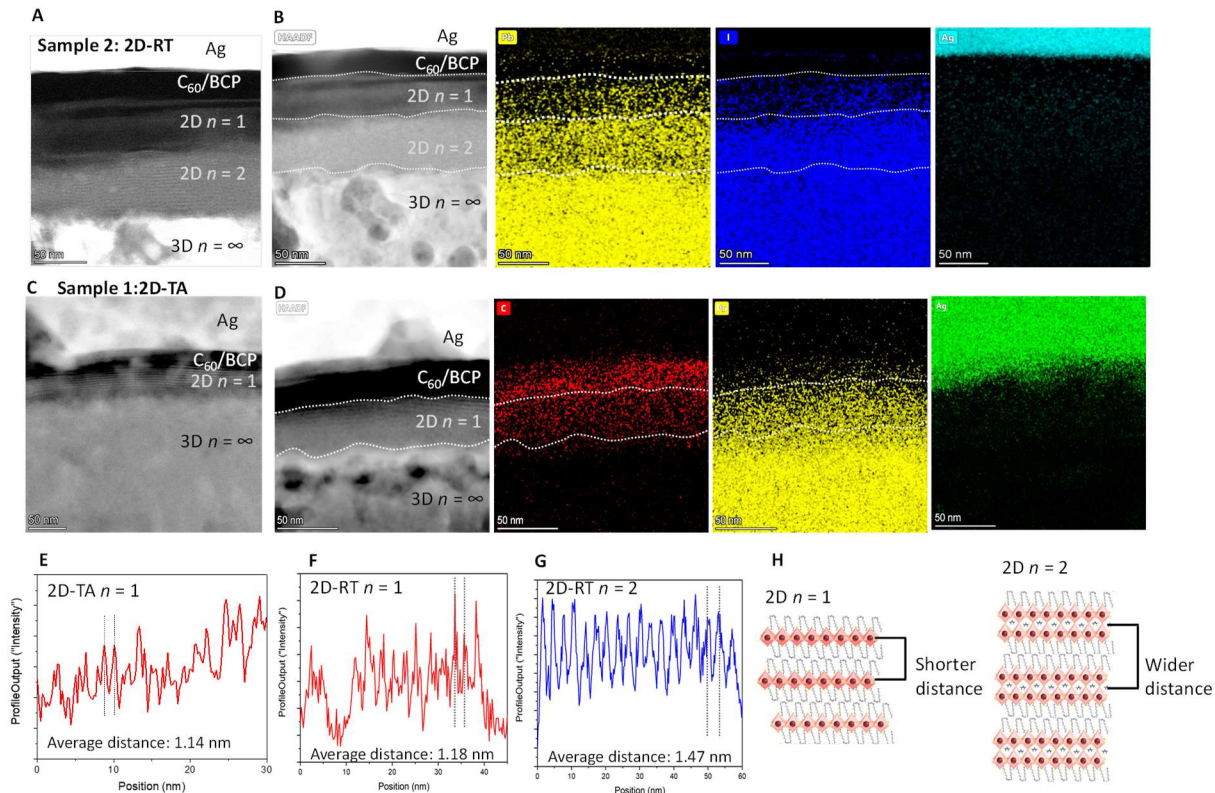
Fig. S2. (A) Cross-sectional STEM images of 2D-RT films of sample number 2 from different batch. It also confirms the gradation of the 2D perovskite dimensionality from $n = 2$ to 1 similar to Fig. 1D in the main-text. **(B)** Elemental map of the cross-sectional STEM image of the 2D-RT of sample number 2 (Pb "yellow color", I "blue color" and Ag "light blue color" from right to left), following results with Fig. 1E. **(C)** Cross-sectional STEM images of sample-1 2D-TA, it shows only one dimensionality. **(D)** Elemental map of the cross-sectional STEM image of 2D-TA sample (C "red color", Pb "yellow color" and Ag "green color" from right to left). It confirms the existence of one dimensionality ($n = 1$) in 2D-TA sample. Profiling position of 2D perovskite with $n = 1$ (red color) and 2 (blue color) layers of **(E)** 2D-TA with $n = 1$, **(F)** 2D-RT with $n = 1$ and **(G)** 2D-RT with $n = 2$. **(H)** Schematic illustration of each octahedral sheet in 2D perovskite layers. It is noted that $n = 1$ layer has a shorter distance compared to $n = 2$ layers. From profiling position analysis, it shows that 2D with n = 1 (red color) has shorter average distance around ~1.2 nm (of both 2D-TA and 2D-RT samples), while 2D with $n = 2$ (blue color) has wider average distance around ~1.5 nm (only on 2D-RT sample).
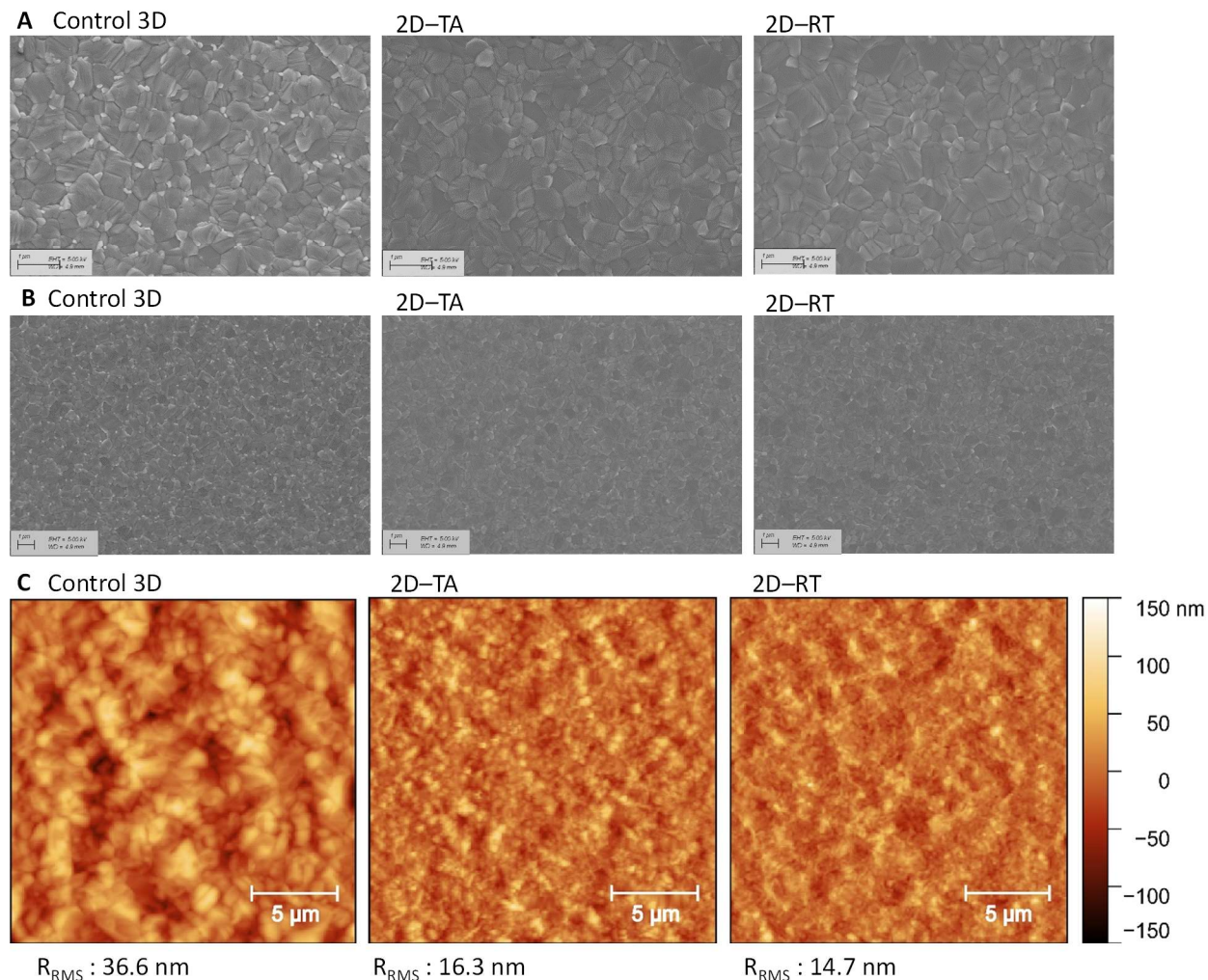
Fig. S3. Morphological properties of perovskite films. Top-view SEM images of perovskite films with and without 2D perovskite passivation at various magnifications, **(A)** 25,000 and **(B)** 10,000 times. Over a large area of SEM images, the PbI$_2$ species (higher contrast) are most likely at grain boundaries of control 3D perovskite films. These PbI$_2$ species were disappeared after OLAI post-treatment (on both 2D-TA and –RT samples), confirming the effective conversion of PbI$_2$ to 2D perovskite layer by post-treatment. The scale bar is 1 µm. **(C)** Atomic force microscopy images of perovskite films-based control, 2D-TA, and 2D-RT under the area of 20 µm × 20 µm. The 2D perovskite layers help reducing the surface roughness of 3D perovskite films by filling regions close to the grain boundaries, as indicated by reducing the R$_{RMS}$ values.
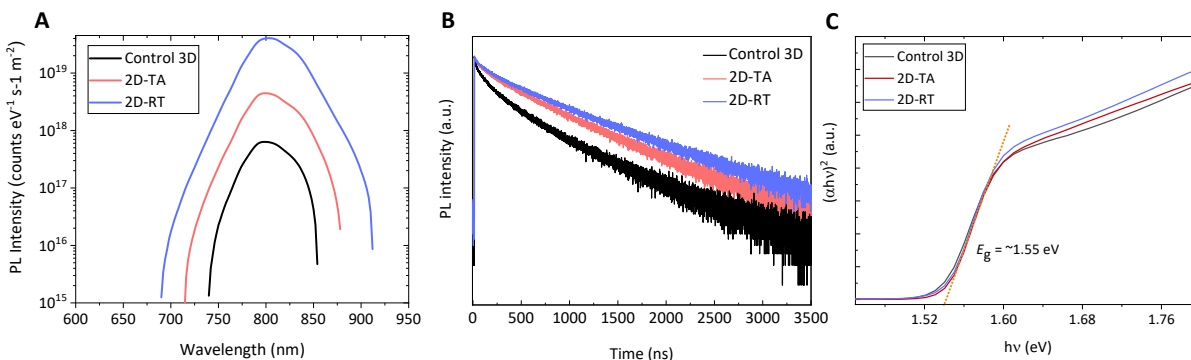
Fig. S4. Optical properties of perovskite films. **(A)** Absolute PL spectra and **(B)** PL decay curves of control- and 2D passivated-based films. The longer decay lifetime in 2D-RT (~699 ns) and 2D passivated-TA (~596 ns) films than the control 3D film (~465 ns) confirmed the suppression of trap states in 3D films by the–NH$_3$ groups and iodide from OLAI molecules, as demonstrated in figure S5. OLAI molecules effectively passivated both cations and anions defects on 3D perovskite surfaces. **(C)** Tauc plot of control and 2D passivated-based films. The optical bandgap of control and after 2D perovskite passivation-based perovskite films remains similar (~1.55 eV).
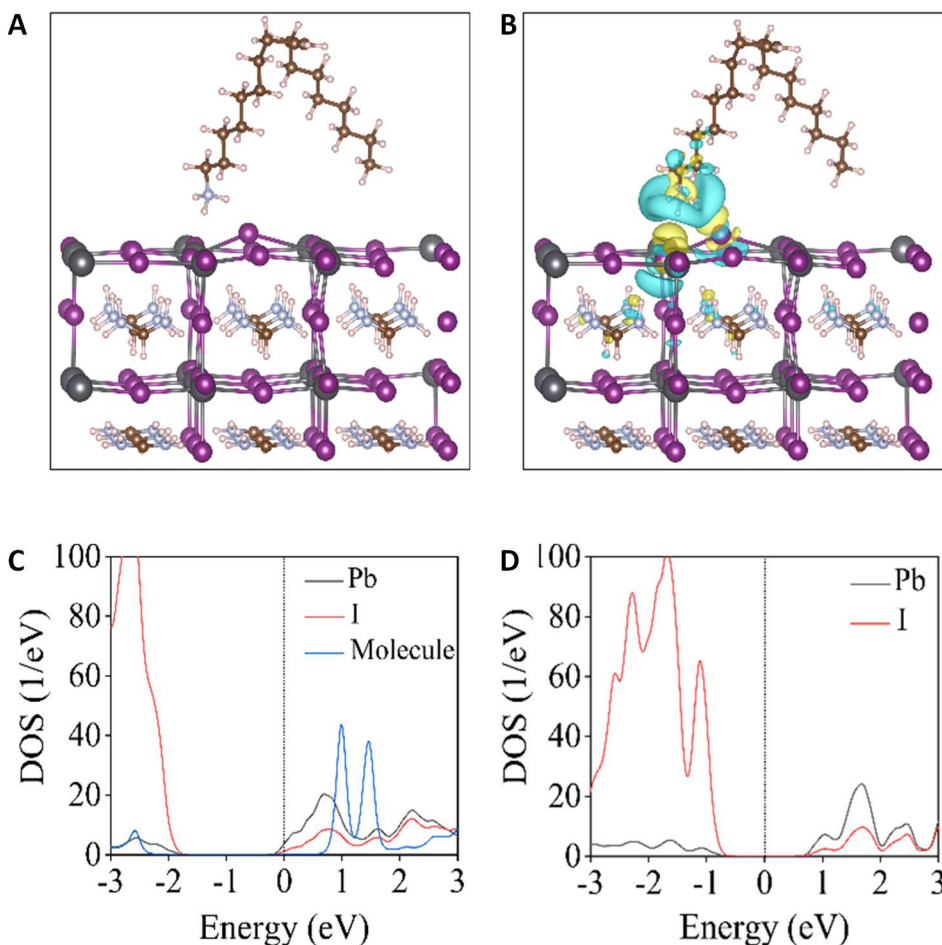
Fig. S5. Density functional theory results. **(A)** Relaxed structure, **(B)** charge density difference, and **(C)** partial densities of states for an oleylammonium molecule on the PbI_2–terminated (001) surface of $FAPbI_3$. **(D)** Partial densities of states of the pristine PbI_2–terminated (001) surface of $FAPbI_3$. Studying various orientations of an oleylammonium molecule on the PbI_2–terminated (001) surface of $FAPbI_3$ by first-principles calculations based on density functional theory, we found that the $–NH_3$ group of the molecule interacts with the Pb and I atoms and that the binding energy is -1.55 eV. The relaxed structure is shown in the panel A. Bader charge analysis demonstrates a transfer of 0.81 electrons from the molecule to $FAPbI_3$. The turquoise and yellow-colored isosurfaces in the panel B represent charge depletion and accumulation regions, respectively, showing that the molecule's interacting end is mainly affected by charge redistribution. Partial densities of states before and after the adsorption of the molecule are compared in the panels C and D. The valence and conduction band edges are found to be dominated by I and Pb, respectively. The charge transfer from the molecule to $FAPbI_3$ results in the occupation of the conduction band in the panel D.
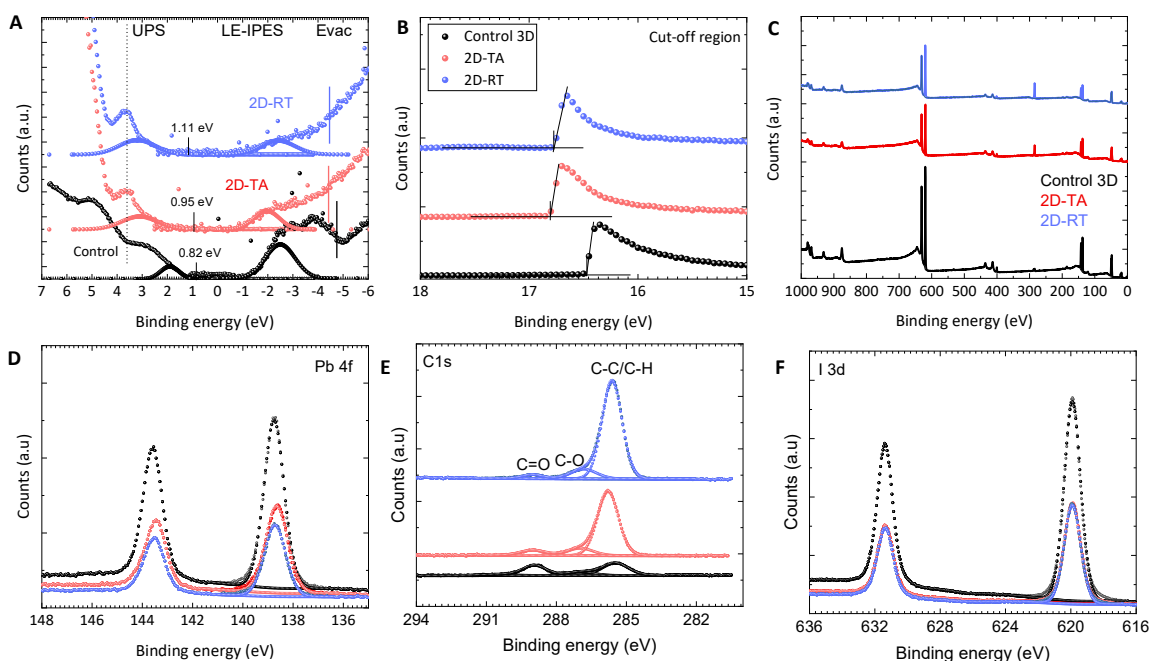
Fig. S6. Ultraviolet photoelectron spectra **(**UPS)/ x-ray photoelectron spectra (XPS) analyses for control and 2D passivated of perovskite films. **(A)** Spectra in the valence band (VB) region and **(B)** secondary electron cut-off plots. (C-F) XPS data of each perovskite film. **(C)** Wide scan range plots, **(D)** Pb4f, **(E)** C1s, and **(F)** I3d of XPS surveys of each sample. The increase in the C-C/C-H peaks on 2D passivated-based films compared to the control film indicates the adequate coverage of 2D ligands on top of 3D films.
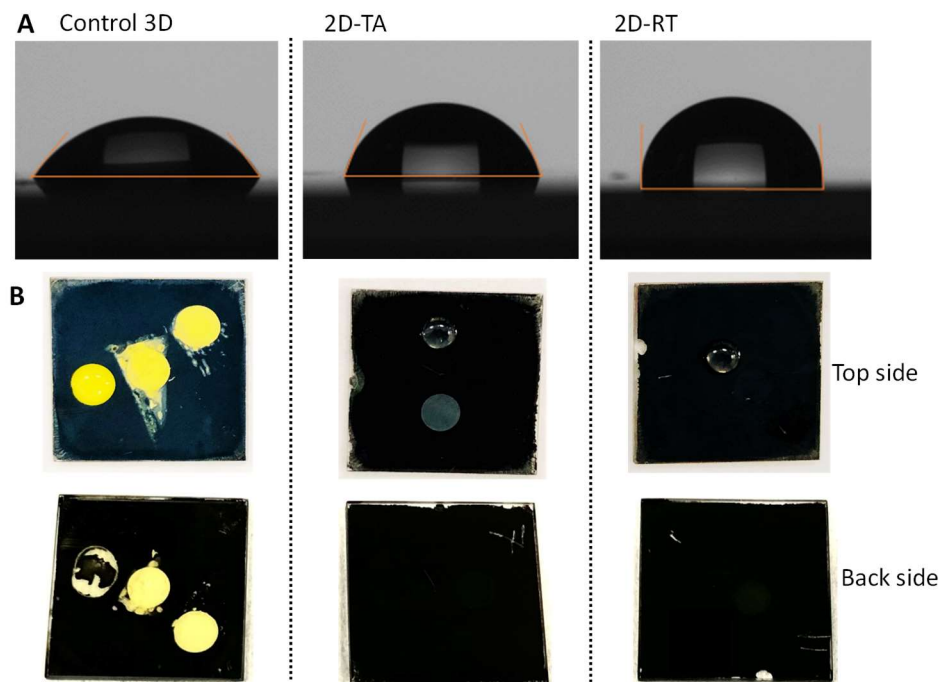
Fig. S7. (A) Water contact angles of control, 2D-TA, and 2D-RT samples. The improved water contact angles of perovskite films for 2D-RT (85.6±1.8°) and TA (71.2±2.1°) compared to control (51.4±2.7°) indicates the coverage of 2D perovskite coatings with long ligand molecules, thus dramatically enhancing the hydrophobicity of the films. The measurements were done with more than five samples with different spots on the films to see the adequate coverage of 2D perovskite layers. **(B)** After a few hours of contact angle measurements, the photograph of control and treated perovskite films from top and backside view. The higher hydrophobicity of the films shows the effectiveness of water droplets blocking into 3D perovskite underneath. Contrastingly, control films demonstrated a reverse reaction to form PbI_2 species that confirms the control 3D perovskite films could not resist the water or humidity ingress.
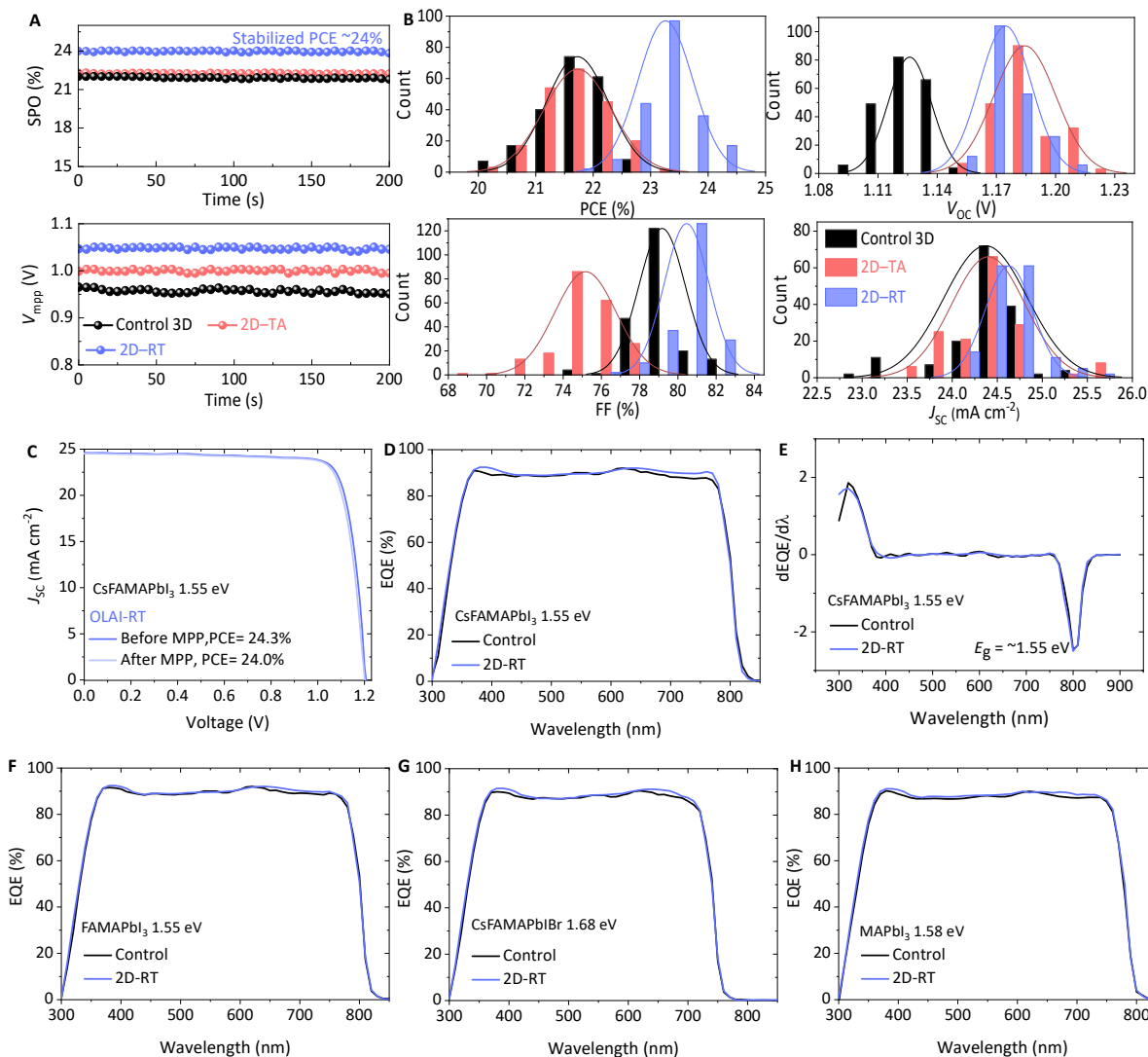
Fig. S8. (A) MPP stabilized power output and voltage maximum, and **(B)** statistical distribution of device performance with and without OLAI treatment. Here, the data reflect 210 pixels of each sample from more than 45 substrates and several subsequent batches. **(C)** *J–V* scan of 2D-RT PSCs before and after MPP measurement in Fig. 3D, confirming the stabilize power output results. **(D)** EQE measurements without white light bias of control and 2D passivated-based inverted PSCs. The integrated J_{SC} values from the EQE analysis exhibit a <2% mismatch compared to that of the J_{SC} values from the *J-V* analysis, confirming the reliability of our analysis results. **(E)** First derivative of the corresponding EQE curves shows that the perovskites have a bandgap of 1.55 eV, following the Tauc plot in fig. S3C. EQE measurements of control and 2D passivated cells with various perovskite composition and bandgap, **(F)** double cation FAMAPbI₃, **(G)** wide-bandgap $Cs_{0.05}FA_{0.80}MA_{0.15}PbI_{2.25}Br_{0.75}$ 1.68 eV and **(H)** MAPbI₃.
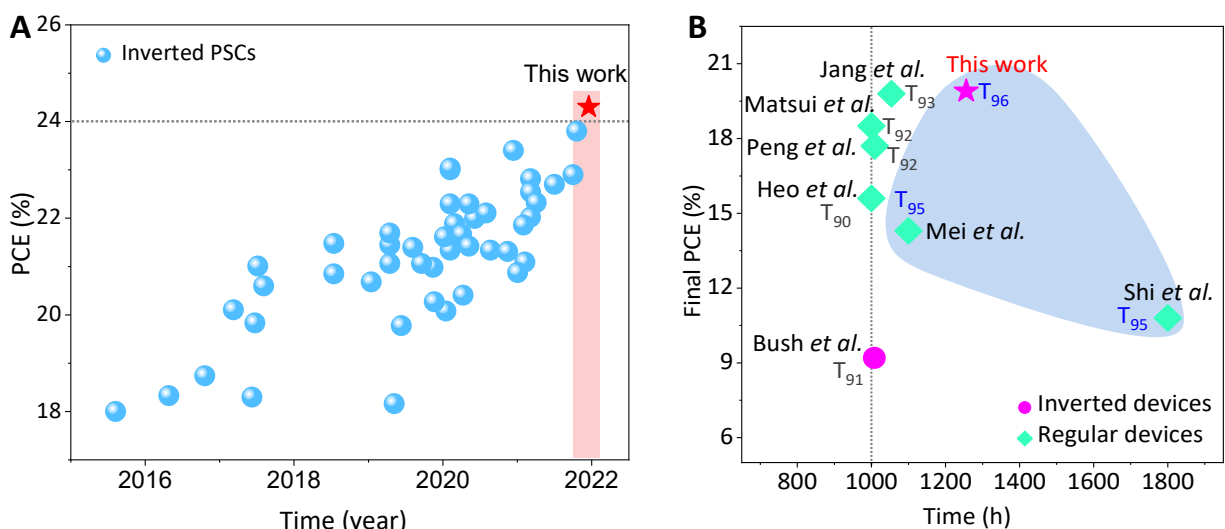
Fig. S9. (A) Summary of reported best PCEs for inverted PSCs from literature compared to the champion PCE 24.3% of this work, as a state-of-the-art PCE among reported inverted PSCs. The data were adopted from fig. S1 in ref. *(26)*. **(B)** Summary of initial and final PCEs of encapsulated PSCs after damp-heat test from literature (tabulated data appear in table S1). The blue marked region shows the successful passing cells for damp-heat tests (IEC 61215:2016).
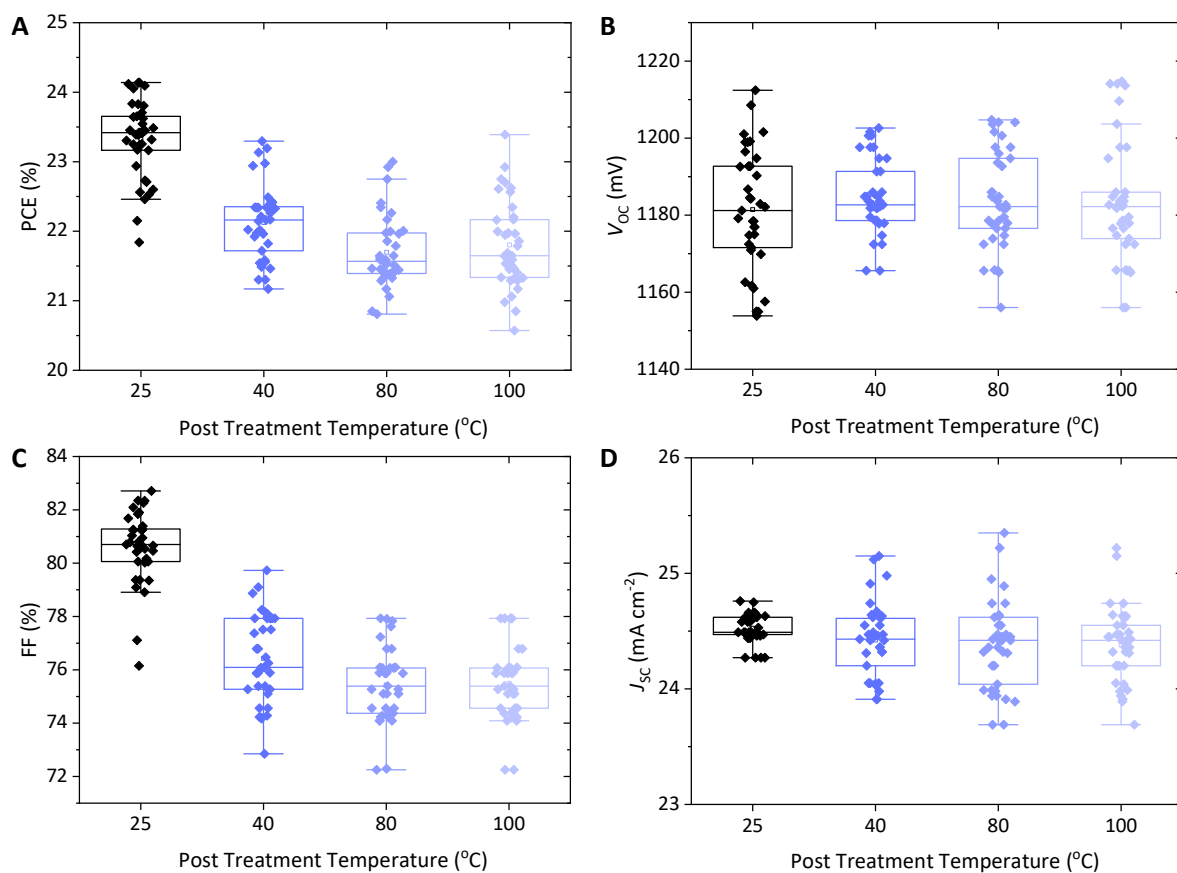
Figure S10. (A-D) Statistics of PCE, V_{OC}, FF, and J_{SC} of 2D-passivated-based PSCs under various temperature annealing (at 25 °C (2D-RT), 40, 80, and 100 °C (2D-TA)) for 10 min. The statistics were collected from 37 pixels of each condition and several subsequent batches.
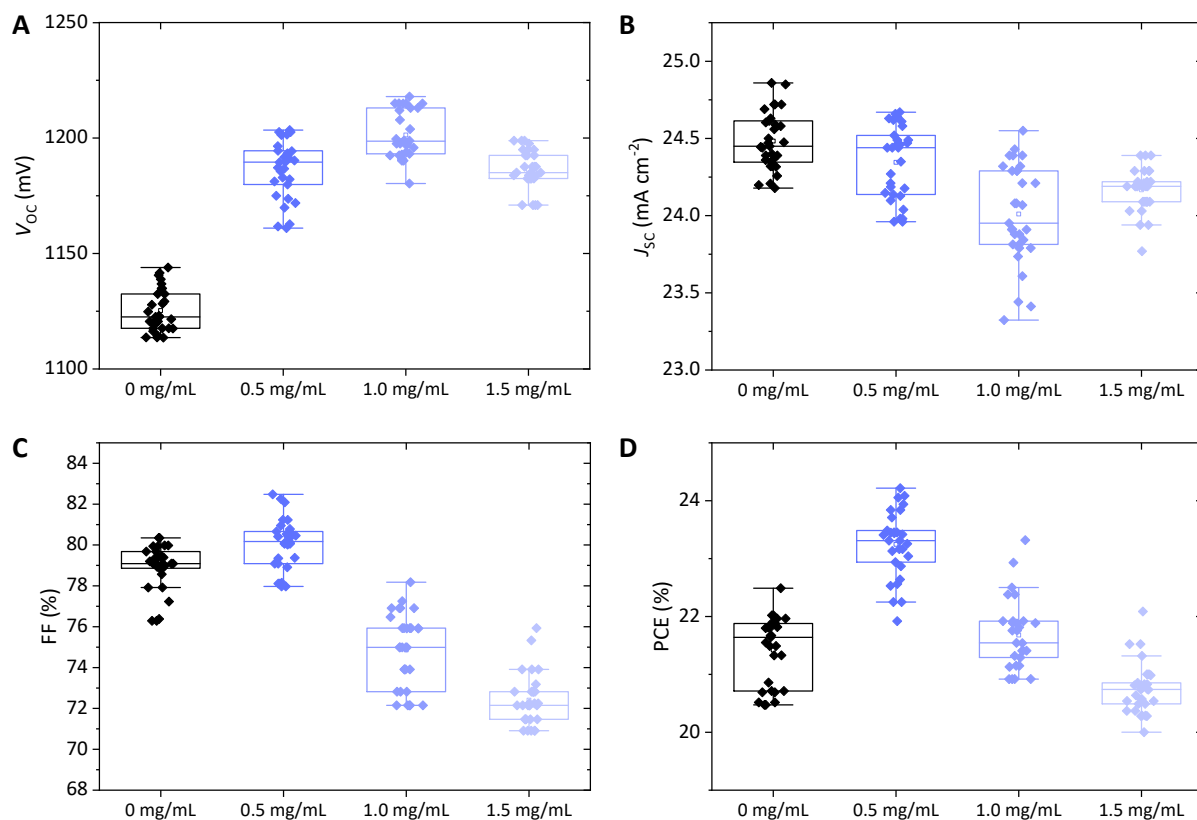
Fig. S11. (A-D) Statistics of V_{OC}, J_{SC}, FF, and PCE of PSCs with different concentrations of 2D OLAI ligands to firstly check the optimum concentration for the 2D passivation. The optimum concentration of OLAI was around 0.5 mg/mL. The statistics were collected from 30 pixels of each condition from several subsequent batches.
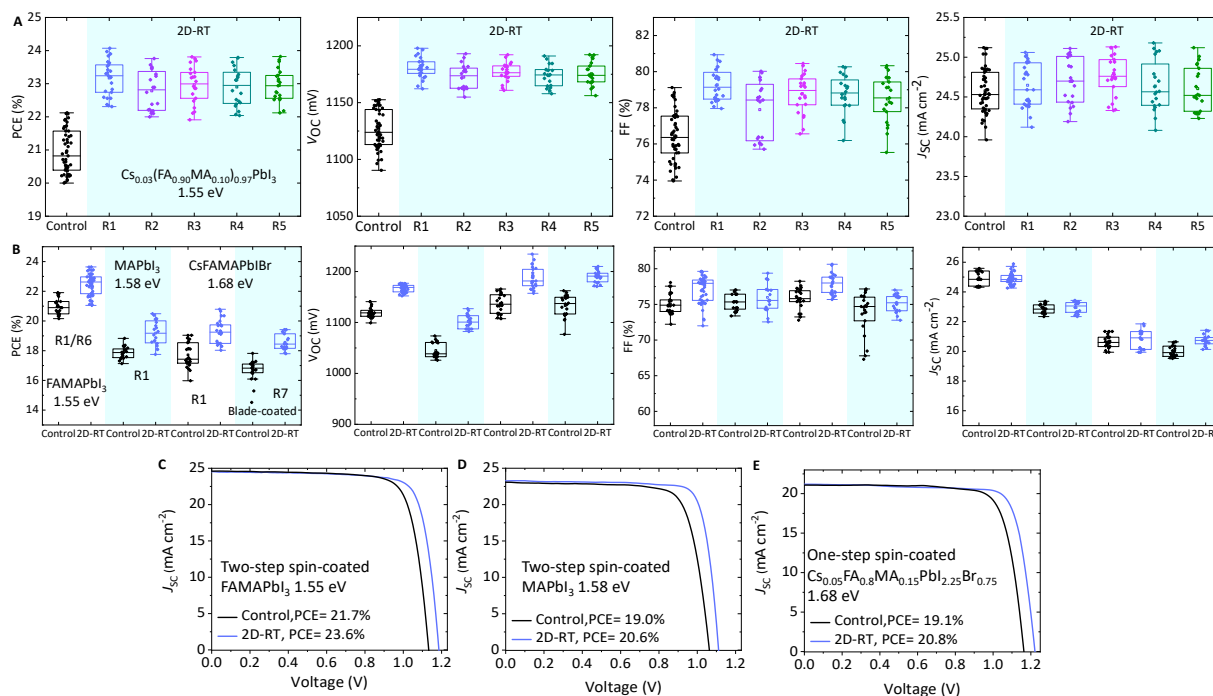
Fig. S12. (A-B) Statistics of V_{OC}, J_{SC}, FF, and PCE of PSCs with different perovskite compositions and bandgaps, also different deposition techniques (spin-coated and blade-coated for wide-bandgap 1.68 eV perovskite). The data were collected from seven different researchers to see the reproducibility of our 2D approach (as denoted as R1-R7). J–V scan of control and 2D passivated-based PSCs under reverse scan with different perovskite compositions and bandgaps, **(C)** double-cation (two-step processes) perovskite-based FAMAPbI$_3$ (with the optical bandgap 1.55 eV); **(D)** two-step processes MAPbI$_3$ perovskite; and **(E)** one-step process triple-cation perovskite-based Cs$_{0.05}$FA$_{0.8}$MA$_{0.15}$PbI$_{2.25}$Br$_{0.75}$ (with the optical bandgap 1.68 eV) by spin-coated, under reverse scan. The bandgap values were obtained from EQE plots in fig S8.(D-G)
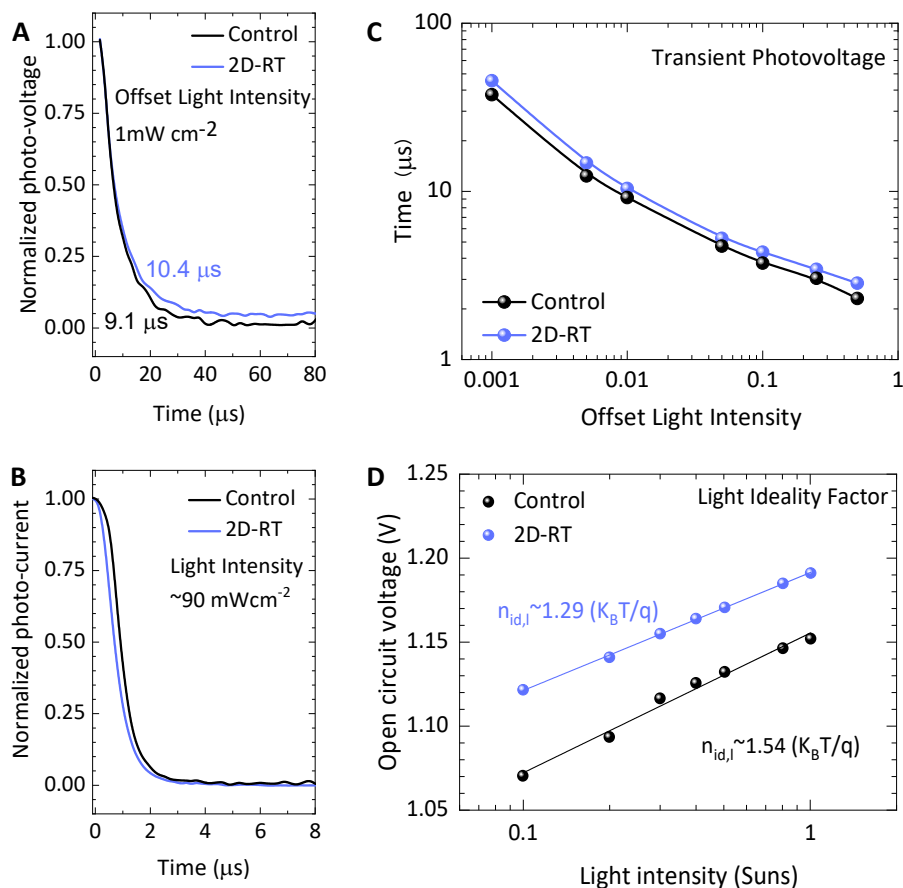
Fig. S13. (A) Transient photo-voltage and **(B)** photo-current measurements illustrating the current/voltage decay of control and 2D passivated devices. The charge transport time (τ_{CT}) and charge recombination lifetime (τ_{rec}) were extracted from decay curves using mono-exponential decay functions. **(C)** τ_{rec} at different light intensities. The 2D passivated devices exhibited longer τ_{rec} and shorter τ_{CT} durations than control devices. These results confirmed that trap passivation at 3D/C_{60} interfaces by the 2D perovskite passivation approach effectively improved the charge extraction of PSCs. **(D)** Light Intensity dependent V_{OC} comparison of control and 2D-RT devices and the corresponding light ideality factor extracted using $n_{id} = q/k_B T * \frac{d V_{OC}}{d \ln(\Phi)}$. The slope of V_{OC} versus the light intensity gives kT/q, where k_B, T, and q are the Boltzmann constant, temperature in Kelvin, and the elementary charge, respectively. The larger the kT/q value, the greater the probability of trap-assisted recombination. The plot slope for the 2D passivation-based devices was lower (~1.29 $k_B T/q$) than that of the control-based devices (~1.54 $k_B T/q$), which indicates reduced trap-assisted bimolecular recombination at 3D/C_{60} interfaces.
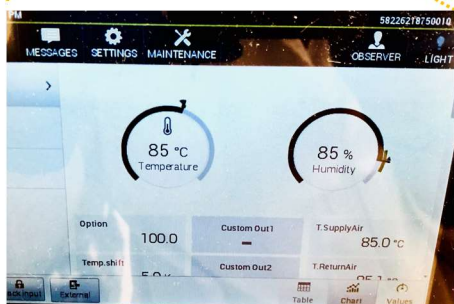
Damp-heat chamber   Inside chamber

Fig. S14. Damp-Heat anti chamber photographs in our lab (KAUST). The temperature and relative humidity levels were maintained at 85 °C and 85%, respectively, following International Electrotechnical Commission (IEC) 61215:2016 standards.
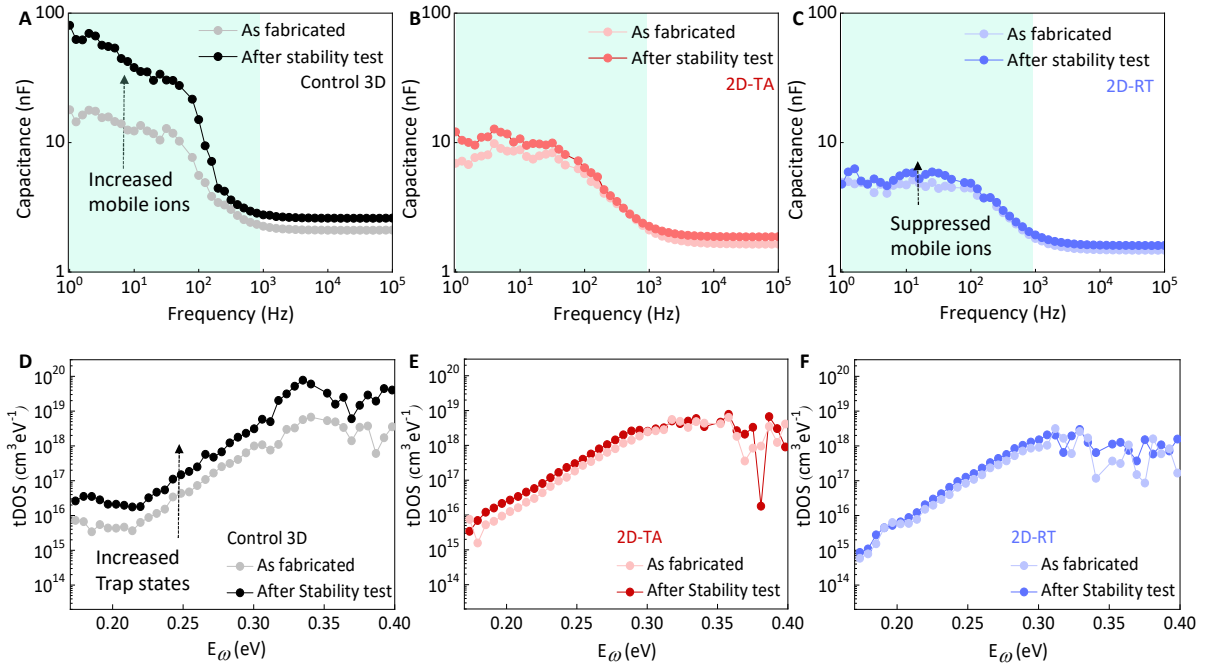
Fig. S15. Ion migrations and trap-states distribution of fresh and aged samples under thermal (85 °C) stress for >500 h in dark. **(A-C)** Capacitance–frequency profiles of control and 2D passivated samples. Electrical poling was performed by applying different biases to the devices with electrodes for 1 min in the dark. Before the measurement, all devices were applied a bias voltage of 2 V to the electrodes by a source meter (Keithley 2400) for about a few minutes to induce the ion migration. All fresh devices have similar capacitance throughout a wide frequency range. However, after the stability test, the control device exhibits a significant increase of capacitance at low frequency (<1 kHz) which is almost one order of magnitude higher than that of the device with 2D perovskite passivation. It is known that the increase of capacitance at low frequency is due to the response of mobile ions in perovskites (*21*). Such a large increase of capacitance in the control device suggests the number of mobile ions within perovskites has been significantly increased, especially after stability stress. Contrastingly, the 2D passivated-based devices did not show any significant change before and after stability stress, suggesting the speculation that the ion dissociation and migration are effectively suppressed by stabilizing 3D perovskite surfaces through the 2D perovskite passivation approach. **(D-F)** Trap density of states (tDOS) deduced from *C–f* plots of each sample. Thermal admittance spectroscopy (TAS) was performed to elucidate the distribution of trap-states in the perovskite layers. It shows *t*DOS (denoted as N_T) with respect to energetic defect levels from TAS, which were obtained from the relation: $N_T (E_\omega) = -(V_{bi} . dC_\omega)/(qW k_B T . d_\omega)$, where C is the capacitance, ω is the angular frequency, *q* is the elementary charge, k_B is Boltzmann's constant, and T is the temperature. It was reported that shallow traps were related to traps in grain boundaries, while deeper traps form primarily at the interfaces or surfaces. The trap density of the control 3D was 10 times higher than that for 2D passivated-based samples. Overall, the tDOS of 2D passivated-based devices has lower tDOS values in all regions (both shallow and deep traps levels), indicating sufficient defect passivation at 3D/C_{60} interfaces.
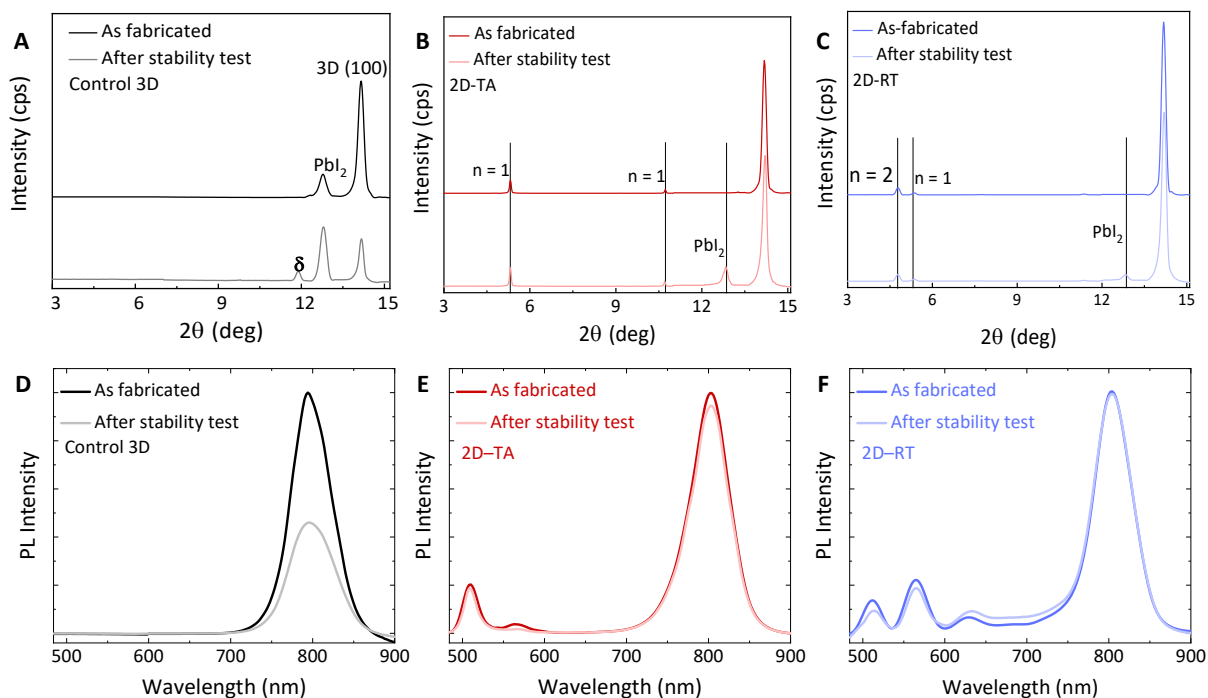
Fig. S16. Structural and optical properties of fresh and aged samples under thermal (85 °C) stress for >500 h in dark. **(A-C)** X-ray diffraction (XRD) patterns of fresh and aged perovskite films. After 2D passivation, the films show no significant changes with only a tiny PbI_2 peak appearance, indicates the effective 2D perovskite capping on 3D perovskite layers. Besides, 2D perovskite peaks were consistently appeared, confirming the robustness of 2D perovskite themselves after a thermal stress test. Contrastingly, the control 3D perovskite films were partially degraded by forming a non-perovskite δ phase and enhanced PbI_2 peak. **(D-F)** Optical emission peaks of fresh and aged perovskite films. The control 3D perovskite films were partially degraded, as indicated by reducing the emission intensity after thermal stress, following the XRD result. Contrastingly, 2D passivated-based films demonstrated more robust emission peak intensity with the same level of intensities at prominent peaks (~802 nm), indicates the effective approach of our 2D perovskite passivation strategy. In addition, the 2D perovskite emission at a shorter wavelength also showed no significant change, indicating a robust 2D perovskite itself, in accordance with the structural XRD patterns results.
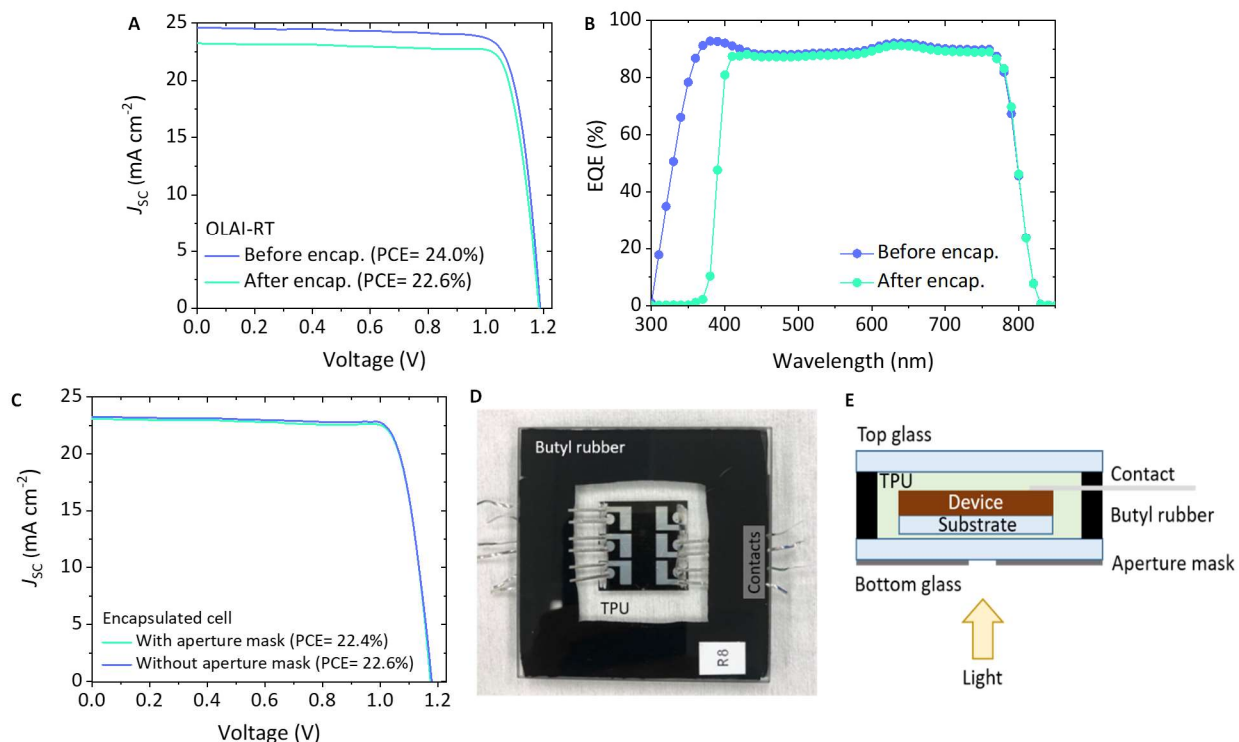
Fig. S17. (A) *J–V* scan and **(B)** EQE plots of 2D-RT-based PSCs before and after encapsulation. The device is encapsulated within two glasses, using thermoplastic polyurethane (TPU) as encapsulant and butyl rubber as edge sealing (see method). The parasitic absorption of the TPU affect the absorption below 380 nm as shown from EQE plots, resulting mainly lower J_{SC} and efficiency of encapsulated devices. **(C)** *J-V* scan of encapsulated devices with and without aperture mask during the measurement. **(D)** Photograph of an encapsulated device from the rear contact. **(E)** Schematic representation of the materials and layers for the encapsulation.
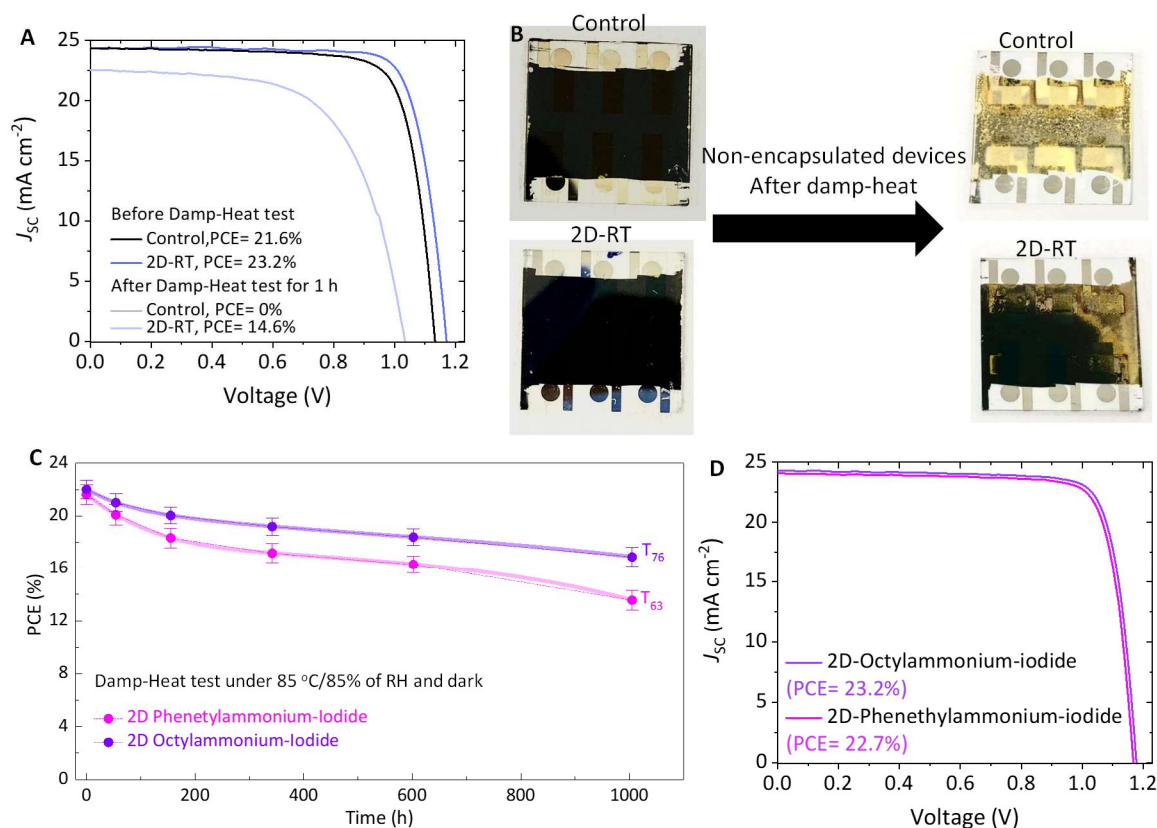
Fig. S18. (A) *J–V* scan of control and 2D-RT passivated-based non-encapsulated devices under damp-heat chamber for 1 hour testing. **(B)** Photograph of control and 2D-RT passivated-based non-encapsulated devices under damp-heat chamber before and after 1 hour testing. **(C)** Comparison of the PCEs at damp-heat test of encapsulated devices-based 2D phenetylammonium-iodide (PEAI) and octylammonium-iodide (OctAI) molecules. **(D)** *J–V* under reverse scan of 2D-PEAI and 2D-OctAI passivation-based non-encapsulated devices. The device structure was ITO/2PACz/3D perovskite/2D perovskite/C_{60}/SnO$_2$/IZO/Ag.
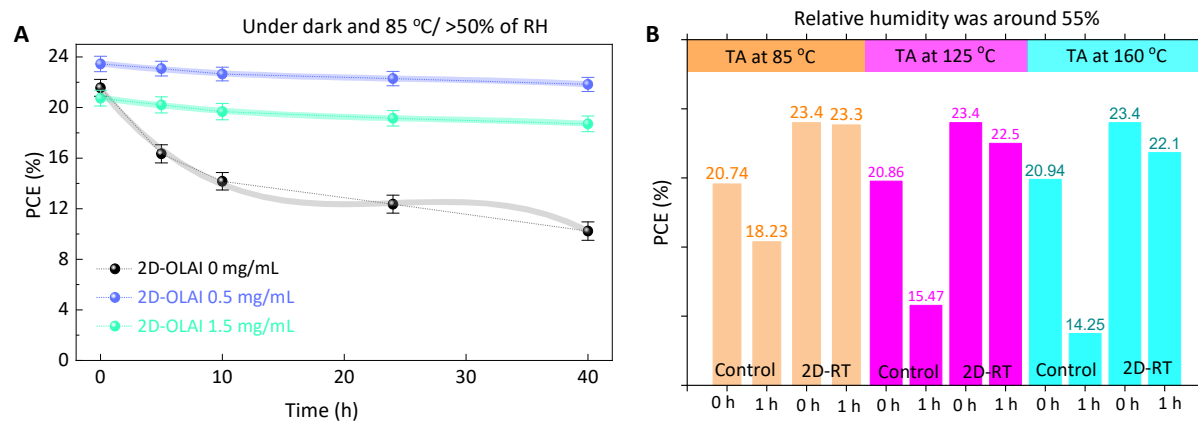
Fig. S19. (A) Evolution of PCE of non-encapsulated devices at 85 ℃ (hot plate) under ambient air with relative humidity was >50% for 40 h test. **(B)** Evolution of PCE of non-encapsulated control and OLAI-treated devices, measured before and after annealing at different temperatures (at 85, 125 and 160 ℃, respectively) in an ambient environment with RH >50%. The annealing time is one hour.

Table S1. Summary of damp-heat (85 °C/85% of relative humidity) stability from literature.

Device configuration	Initial PCE (%)	Damp-Heat 85 °C/85% RH Lifetime/Time	Final PCE (%)	Journal	Ref.
FTO/TiO$_2$/PVK/PPDTFBT:BCF/PEDOT/ITO	17.3	T$_{90}$ for 1000 h	15.6	*Adv. Mater. Tech.*	*(35)*
FTO/TiO$_2$/RbCsFAMAPbIBr/PTAA/Au	20.1	T$_{92}$ for 1000 h	18.5	*Adv. Mater.*	*(36)*
FTO/SnO$_2$/FAMAPbIBr/PTAA/Au	21.3	T$_{93}$ for >1050 h	19.8	*Nat. Energy*	*(3)*
*FTO/TiO$_2$/CsFAMA/PTAA/Au	11.4	T$_{95}$ for >1800 h	10.8	*Science*	*(2)*
*FTO/TiO$_2$/(5-AVA)$_x$MA$_{1-x}$PbI$_3$ /ZrO$_2$/Carbon	~15	T$_{95}$ for 1100 h	14.3	*Joule*	*(1)*
ITO/TiO$_2$/CsFAMA/P3HT/MOO$_x$/IZO/Au	19.3	T$_{92}$ for >1000 h	17.7	*Science*	*(37)*
ITO/NiO$_x$/CsFAPbIBr/LiF/PCBM/SnO$_2$/ITO/Ag	10.1	T$_{91}$ for 1008 h	9.2	*Nat. Energy*	*(38)*
*ITO/NiO$_x$-KCl/Cs$_{0.07}$FA$_{0.93}$PbI$_3$/C$_{60}$/SnO$_2$/IZO/Ag	20.3	T$_{96}$ for >1250 h	19.9	-	This work

*The symbol indicates the successful passing cells for damp-heat (IEC61215:2016) test after >1000 h with less than 5% efficiency loss.